Physics – Uspekhi **42** (8) 779 – 796 (1999)

REVIEWS OF TOPICAL PROBLEMS PACS numbers: 61.10.Ht, 75.25.+z, **75.70.i**, 78.20.Ls

Application of synchrotron radiation to the study of magnetic materials

S G Ovchinnikov

Contents

Abstract. Recent results of studies of magnetic materials using synchrotron radiation are reviewed. The influence of magnetic effects on X-ray scattering is studied for linearly and circularly polarized photons, and the effects of magnetic circular dichroism on the spectra of X-ray absorption and photoelectron emission are discussed. It is shown that X-ray magnetooptic techniques provide fine detail of crystal and magnetic structures and also make it possible to separate the spin and orbital contributions to the total moment; to obtain element- and position-sensitive information on the magnetic properties of the material; to visualize domains and domain walls; and to probe magnetization reversal dynamics. A comparison of magnetic neutron and X-ray methods is given.

1. Introduction

The use of X-rays for the study of the magnetic properties of matter began comparatively recently. The first results on X-ray magnetic diffraction were published in 1972 [1], and the first experiments on magnetic circular dichroism were conducted in the late 80s. The progress of this line of investigation is determined by the application of synchrotron radiation as a high-brilliance source of photons with excellent polarization characteristics.

The measurement of magnetic contributions in the diffraction peaks (1/2, 1/2, 1/2) and (3/2, 3/2, 3/2) for NiO with the use of the standard X-ray tubes, as was done by the author of the paper [1], is an extremely complicated experiment. The matter is that the magnetic cross section is less than the charge cross section by a factor $\left[\hbar\omega/(mc^2)\right]^2 \approx 4 \times 10^{-4}$ for X-rays with an energy of $\hbar\omega = 10$ keV. Taking into account other contributions decreasing the magnetic cross section (the number of unpaired electrons, the average spin, and so on), leads to the fact that in NiO charge scattering turns out to be 10^7 times larger than the magnetic scattering. Thus, magnetic X-ray scattering exists, it can be measured, but it is very weak compared with charge scattering.

Two factors have contributed to the fact that this weak scattering is evolving before our eyes into a powerful and informative instrument for the investigation of magnetic structures. The first factor is the development of synchrotron radiation (SR) sources in the 70s and 80s. Owing to the high intensity of SR, the weakness of magnetic scattering characterized by a factor of $10^{-4} - 10^{-7}$ can be partially compensated. An additional advantage of SR is the high degree of polarization: presently, the linear polarization in the plane of the synchrotron can be as much as 99%. Rotating the plane of polarization through $\pi/2$ is often used to separate magnetic scattering.

The second factor is the discovery of resonance X-ray scattering [2, 3]; in the vicinity of specific values of intra-atomic absorption energies, the scattering cross section is very sensitive to the value of the photon energy, which results in a considerable increase of the magnetic signal (by a factor of ~ 100 for lanthanides and 10^6 for actinides). X-ray resonance magnetic scattering (XRMS) is determined by electric multipole effects (dipole and quadrupole) and, owing to the Pauli exclusion principle, is sensitive to electron spins. Resonance effects have been also found in X-ray absorption: magnetic circular dichroism (MCD) [4] and the spin-dependent absorption of circularly polarized SR [5] can be used for the investigation of magnetism.

S G Ovchinnikov L V Kirenskiĭ Institute of Physics, Siberian Division, Russian Academy of Sciences
Akademgorodok, 660036 Krasnoyarsk, Russian Federation
Tel. (7-3912) 43 29 06. Fax (7-3912) 43 89 23
E-mail: sgo@post.krascience.rssi.ru

Received 4 February 1999, revised 11 May 1999
Uspekhi Fizicheskikh Nauk **169** (8) 869 – 887 (1999)
Translated by V M Matveev; edited by S N Gorin

During the last decade, X-ray magnetooptics has been developing vigorously. A variety of methods, beginning with nonresonance magnetic diffraction (which enables one to separate the orbital and spin parts of the magnetic form factor) and ending with resonance scattering (which gives element-sensitive information, including information from surface and ultrathin layers) and MCD (which makes it possible to observe the dynamic behavior of magnetic inhomogeneities). Scattering and absorption experiments with circularly and linearly polarized SR are conducted. The use of linearly polarized SR for the investigation of magnetic structures provides high resolution in the k space and is applied to antiferromagnets, superlattices, and thin ferromagnetic layers [6]. For circularly polarized photons, there exists an interference of charge and magnetic elastic scattering found experimentally in work [7]. The scattering of SR with a linear and circular polarization can be used for separating spin and orbital contributions to a magnetic moment. In experiments on absorption of linearly polarized radiation [8] the strong polarization dependence of the 3d absorption spectra of rare-earth metals (REM) was found. A spin-dependent part of absorption for circularly polarized radiation was first found for ferromagnetic iron [5]. The investigation of MCD in XANES (X-ray Absorption Near-Edge Structure) and EXAFS (Extended X-ray Absorption Fine Structure) spectra have become a powerful tool for studies of the element- and symmetry-sensitive characteristics of the local electronic structure in magnetic materials [9].

The goal of this work is to review the present state of X-ray magnetooptics of magnetic materials, new methods for the investigation of such materials and the results of applying these methods to concrete substances. As is often the case in solid state physics, the interpretation of results is rather simple and reliable in the two limiting cases: for the interactions of photons with localized electrons, when the atomistic approach is possible, and for their interactions with itinerant electrons in metals, when the band theory is applicable. In the intermediate cases, when the Coulomb energy of the electron–electron interaction is comparable with the kinetic energy of electrons, the proper interpretation of X-ray magnetooptics data requires a further development of the theory. At the same time, X-ray magnetooptics is of importance not only for fundamental investigations.

The complicated interplay of the electron structure, magnetic properties, thin-film morphology, lithographic processes, and the magnetization-reversal dynamics of new magnetic materials and related devices interpose obstacles to the successful application of these new materials in magnetic-memory devices and magnetic sensors. It is characteristic of these devices that they are multilayer, multielement and heteromagnetic (containing more than one magnetic element) devices. For the most part, the standard magnetic methods provide integrated information on the properties of materials; therefore, the appearance of new X-ray magnetooptic methods, making it possible to study individual elements and layers, is undeniably useful for the optimization and development of new magnetic devices.

2. Magnetic effects in the interaction of X-rays with matter

In solid state physics, the traditional point of view is that X-ray scattering provides information on the charge density. Indeed, the charge density makes the main contribution to the scattering cross section. At the same time, the following (lesser) terms contain information on the magnetic moment [10]. Theoretical predictions concerning the possibility of using X-ray scattering for determination of the magnetic structure of matter were argued in the papers [11–14]. As is known, in the weak nonrelativistic limit, when the photon energy is small in comparison with the electron rest energy ($\hbar\omega/(mc^2) \ll 1$), the Hamiltonian of the interaction of an electromagnetic field with a system of electrons can be written in the form [14]

$$\begin{aligned} H' &= \frac{e^2}{2mc^2}\sum_j A^2(\mathbf{r}_j) - \frac{e}{2mc}\sum_j \mathbf{A}(\mathbf{r}_j)\cdot\mathbf{p}_j \\ &\quad - \frac{e\hbar}{2mc}\sum_j \mathbf{S}_j\cdot\left[\boldsymbol{\nabla}\times\mathbf{A}(\mathbf{r}_j)\right] \\ &\quad - \frac{e^2\hbar}{2(mc^2)^2}\sum_j \mathbf{S}_j\cdot\left[\frac{\partial\mathbf{A}(\mathbf{r}_j)}{\partial t}\times\mathbf{A}(\mathbf{r}_j)\right] \\ &= H_1' + H_2' + H_3' + H_4' , \end{aligned} \tag{1}$$

where $\mathbf{A}(\mathbf{r}_j)$ is the vector potential of the field at the point $\mathbf{r}_j$, and $\mathbf{S}_j$ is the spin of the jth electron with a momentum $\mathbf{p}_j$. The meaning of the four terms in Eqn (1) is as follows: the first two terms are connected with the kinetic energy, the third term describes the Zeeman interaction of the electron spin with the magnetic field of a wave, and the last term is determined by the spin–orbit interaction.

2.1 General formulas for magnetic X-ray scattering [1]

An X-ray scattering experiment is associated with a two-photon process in which an incident photon with an energy $\hbar\omega_i$, wave vector $\mathbf{k}_i$ and polarization $\boldsymbol{\varepsilon}_i$ is annihilated and a photon in a final state with an energy $\hbar\omega_f$, wave vector $\mathbf{k}_f$ and polarization $\boldsymbol{\varepsilon}_f$ is ejected. The terms $H_1' + H_4'$ in the Hamiltonian contribute even in the first order of the perturbation theory, since these terms contain two operators $\mathbf{A}$ each, and the terms $H_2' + H_3'$ contain only one operator $\mathbf{A}$ and contribute only in the second order of the perturbation theory. Introducing the initial and final states of the system

$$|i\rangle = |0_e; \mathbf{k}_i, \boldsymbol{\varepsilon}_i\rangle, \qquad |f\rangle = |f_e; \mathbf{k}_f, \boldsymbol{\varepsilon}_f\rangle \tag{2}$$

(where the ground and excited states of the electron system are designated as 0_e and f_e) with the energies of the initial and final states $\epsilon_i = E_{0e} + E_i$, $\epsilon_f = E_{f_e} + E_f$ in the form of the sum of the electron and photon energies, we can write the probability of scattering in the form

$$\begin{aligned} \omega_{i\to f} = \frac{2\pi}{\hbar}\Bigg| &\langle f|H_1' + H_4'|i\rangle \\ &+ \sum_n \frac{\langle f|H_2' + H_3'|n\rangle\langle n|H_2' + H_3'|i\rangle}{\epsilon_i - \epsilon_n}\Bigg|^2 \delta(\epsilon_i - \epsilon_f) . \end{aligned} \tag{3}$$

The doubly differential scattering cross section is connected with the measurable quantities

$$\frac{\mathrm{d}^2\sigma}{\mathrm{d}E_f\,\mathrm{d}\Omega_f} = r_0^2\,\frac{\omega_f}{\omega_i}\sum_{f_e} |M_{if}|^2 \delta(E_{0e} - E_{f_e} + \hbar\omega_i - \hbar\omega_f) , \tag{4}$$

[1] This section has been written based on the material of M Altarelli's lecture [15].

where $r_0 = e^2/(mc^2) = 2.82 \times 10^{-13}$ cm is the classical electron radius, and the scattering amplitude is [14]

$$M_{if} = \left\langle f \left| \sum_j \exp(\mathrm{i}\mathbf{Q}\mathbf{r}_j) \right| i \right\rangle (\boldsymbol{\varepsilon}_f^* \cdot \boldsymbol{\varepsilon}_i)$$
$$- \mathrm{i}\,\frac{\hbar\omega_i}{mc^2} \left\langle f \left| \sum_j \exp(\mathrm{i}\mathbf{Q}\mathbf{r}_j)\mathbf{S}_j \right| i \right\rangle (\boldsymbol{\varepsilon}_f^* \times \boldsymbol{\varepsilon}_i)$$
$$+ \frac{1}{m} \sum_{jl} \left(\sum_n \left\{ \frac{\langle f | \left[\boldsymbol{\varepsilon}_f^* \cdot \mathbf{p}_j - \mathrm{i}\hbar(\mathbf{k}_f \times \boldsymbol{\varepsilon}_f) \cdot \mathbf{S}_j \right] \exp(-\mathrm{i}\mathbf{k}_f \mathbf{r}_j) | n \rangle}{E_i - E_n + \hbar\omega_i - \mathrm{i}\Gamma_n/2} \right.\right.$$
$$\left.\left. \times \langle n | \left[\boldsymbol{\varepsilon}_i \cdot \mathbf{p}_l + \mathrm{i}\hbar(\mathbf{k}_i \times \boldsymbol{\varepsilon}_i) \cdot \mathbf{S}_l \right] \exp(\mathrm{i}\mathbf{k}_i \mathbf{r}_l) | i \rangle \right\} \right.$$
$$\left. + \sum_{n'} \left\{ \frac{\langle f | \left[\boldsymbol{\varepsilon}_i^* \cdot \mathbf{p}_j + \mathrm{i}\hbar(\mathbf{k}_i \times \boldsymbol{\varepsilon}_i) \cdot \mathbf{S}_j \right] \exp(\mathrm{i}\mathbf{k}_i \mathbf{r}_j) | n' \rangle}{E_i - E_{n'} - \hbar\omega_f} \right.\right.$$
$$\left.\left. \times \langle n' | \left[\boldsymbol{\varepsilon}_f \cdot \mathbf{p}_l - \mathrm{i}\hbar(\mathbf{k}_f \times \boldsymbol{\varepsilon}_f) \cdot \mathbf{S}_l \right] \exp(-\mathrm{i}\mathbf{k}_f \mathbf{r}_l) | i \rangle \right\} \right) . \quad (5)$$

Here, the scattering vector $\mathbf{Q} = \mathbf{k}_i - \mathbf{k}_f$ is introduced; the indices j, l run over all electron states. The summation over the intermediate states is broken down into two terms: in the first, $|n\rangle$, a photon $\hbar\omega_i$ is annihilated, and there are no other photons; in the second, $|n'\rangle$, a photon $\hbar\omega_f$ is created, and both photons are present. In the first case a resonance state at $E_i - E_n + \hbar\omega_i \to 0$ is possible, and the imaginary part $\mathrm{i}\Gamma_n/2$ is introduced to account for a finite lifetime of the corresponding intermediate state. Equation (5) takes into account all cases of interest to us, namely, elastic, inelastic, nonresonance, and resonance X-ray scattering.

First we consider the case of nonresonance scattering, when $\hbar\omega_i \gg E_n - E_i$ for all the relevant intermediate states. Here, the first term in Eqn (5) (corresponding to H_1') is dominant. It gives the following scattering cross section:

$$\frac{\mathrm{d}^2\sigma}{\mathrm{d}E_f\,\mathrm{d}\Omega_f} = r_0^2 \frac{\omega_f}{\omega_i} (\boldsymbol{\varepsilon}_f^* \cdot \boldsymbol{\varepsilon}_i)^2 S(\mathbf{Q}, \omega) , \quad (6)$$

where the dynamical structure factor can be written through the correlation function of the electron density $\rho(\mathbf{r}, t)$

$$S(\mathbf{Q}, \omega) = \frac{1}{2\pi\hbar} \int_{-\infty}^{\infty} \mathrm{d}\mathbf{r}\,\mathrm{d}\mathbf{r}'\,\mathrm{d}t \exp(-\mathrm{i}\omega t)$$
$$\times \exp\left[-\mathrm{i}\mathbf{Q}(\mathbf{r} - \mathbf{r}')\right] \langle i | \rho(\mathbf{r}, 0)\rho(\mathbf{r}', t) | i \rangle . \quad (7)$$

For elastic scattering, we have $\omega = 0$; therefore, we obtain the well-known Bragg–Thomson formula for charge scattering used in crystallography.

(1) **Magnetic X-ray elastic nonresonance scattering** is described by the next-smallest terms in Eqn (5), which can be written in the form [14]

$$\frac{\mathrm{d}^2\sigma}{\mathrm{d}E_f\,\mathrm{d}\Omega_f} = r_0^2 \left| \left\langle f \left| \sum_j \exp(\mathrm{i}\mathbf{Q}\mathbf{r}_j) \right| i \right\rangle (\boldsymbol{\varepsilon}_f^* \cdot \boldsymbol{\varepsilon}_i) \right.$$
$$- \mathrm{i}\,\frac{\hbar\omega_i}{mc^2} \left\{ \frac{mc}{e\hbar} \frac{\langle i | \mathbf{Q} \times \left[\mathbf{M}_L(\mathbf{Q}) \times \mathbf{Q} \right] | i \rangle}{\mathbf{Q}^2} \cdot \mathbf{P}_L \right.$$
$$\left. \left. + \frac{mc}{e\hbar} \langle i | \mathbf{M}_S(\mathbf{Q}) | i \rangle \cdot \mathbf{P}_S \right\} \right|^2 , \quad (8)$$

where $\mathbf{M}_L(\mathbf{Q})$ and $\mathbf{M}_S(\mathbf{Q})$ are the Fourier transforms of the orbital and spin magnetic moment densities, respectively, and the polarization factors $\mathbf{P}_L$ and $\mathbf{P}_S$ are

$$\mathbf{P}_L = (\boldsymbol{\varepsilon}_f^* \times \boldsymbol{\varepsilon}_i)\, 4 \sin^2 \Theta_\mathrm{B} , \quad (9)$$

$$\mathbf{P}_S = \boldsymbol{\varepsilon}_f^* \times \boldsymbol{\varepsilon}_i + \frac{1}{k^2} \left[(\mathbf{k}_f \times \boldsymbol{\varepsilon}_f^*)(\mathbf{k}_f \cdot \boldsymbol{\varepsilon}_i) - (\mathbf{k}_i \times \boldsymbol{\varepsilon}_i)(\mathbf{k}_i \cdot \boldsymbol{\varepsilon}_f^*) \right.$$
$$\left. - (\mathbf{k}_f \times \boldsymbol{\varepsilon}_f^*) \times (\mathbf{k}_i \times \boldsymbol{\varepsilon}_i) \right] . \quad (10)$$

In the case of elastic scattering, $k = |\mathbf{k}_i| = |\mathbf{k}_f|$, and the scattering angle (between the vectors $\mathbf{k}_i$ and $\mathbf{k}_f$) is designated as $2\Theta_\mathrm{B}$. Whereas the first term in Eqn (8) is due to charge scattering, the second and third ones, containing a small factor $\hbar\omega_i/(mc^2)$, depend on the magnetic moment. Note that owing to the difference of the polarization factors ($\mathbf{P}_L \neq \mathbf{P}_S$), the orbital and spin moments contribute differently to the scattering cross section, which makes it possible to determine them individually at the appropriate experimental geometry.

The direct measurement of magnetic contributions in the scattering of linearly polarized photons is possible in antiferromagnets, where the magnetic and charge scattering are separated in the k space. Is it possible to measure a weak magnetic contribution in ferromagnets where it exists against the background of a strong peak from charge scattering? It turns out that it is. For circularly polarized synchrotron radiation, one can induce the interference of the charge and magnetic scattering amplitudes, which enables one to separate the magnetic intensity in non-steady-state experiments. It is necessary either to change periodically the sign of polarization (right to left and vice versa) or to reverse periodically the magnetization of the sample. In practice, the latter method is used more often.

(2) **Magnetic resonance elastic scattering.** In this case, $E_i - E_n + \hbar\omega_i \to 0$ and the third term in Eqn (5) is dominant. The resonance condition implies that the energy of the γ quantum is close to the energy of an intermediate state with a hole in the inner atomic shell and an electron above the Fermi level. As was mentioned by the authors of the papers [2, 3], the resonance conditions make preferable a small number of intermediate states $|n\rangle$ with energies close to $\hbar\omega_i$. For a magnetically ordered system, the one-electron states with spin up and spin down are characterized by different occupation numbers and energies and therefore are variously accessible for virtual excitation from the inner shells. A convenient form of writing the resonance scattering is suggested in Ref. [3], where the spherical components of the radius vector $\mathbf{r} = (R_0, R_{+1}, R_{-1})$, $R_0 = \mathrm{i}z$, $R_{\pm 1} = \mp\mathrm{i}/\sqrt{2}(x \pm \mathrm{i}y)$ are introduced and the scattering cross section is written in the form

$$\frac{\mathrm{d}^2\sigma}{\mathrm{d}E_f\,\mathrm{d}\Omega_f} = r_0^2 \left| \sum_{\mathbf{R}} \exp(\mathrm{i}\mathbf{Q}\mathbf{R}) \left[\frac{1}{2} (\boldsymbol{\varepsilon}^* \cdot \boldsymbol{\varepsilon})(F_{1,1} + F_{1,-1}) \right.\right.$$
$$- \frac{\mathrm{i}}{2} (\boldsymbol{\varepsilon}^* \times \boldsymbol{\varepsilon}) \cdot \mathbf{z}_R (F_{1,1} + F_{1,-1})$$
$$\left.\left. + (\boldsymbol{\varepsilon}^* \cdot \mathbf{z}_R)(\boldsymbol{\varepsilon} \cdot \mathbf{z}_R) \left(F_{1,0} - \frac{F_{1,1}}{2} - \frac{F_{1,-1}}{2} \right) \right] \right|^2 . \quad (11)$$

Here, $\mathbf{z}_R$ is the unit vector along the quantization axis coinciding with the local direction of magnetization, and

$$F_{1,q} = \frac{m}{\hbar^2} \sum_n (E_i - E_n)^2 \frac{\left| \langle n | R_q | i \rangle \right|^2}{E_i - E_n + \hbar\omega_i + \mathrm{i}\Gamma_n/2} . \quad (12)$$

Expression (11) was obtained for a system of magnetic ions that are placed in a weak crystal field and hold the rotational

symmetry of the atom. This approximation is reasonable for the 4f electrons of REM, but less substantiated for 3d metals. In this expression, the dependence of the scattering cross section on the number of the shell from which an electron was excited is seen. Since it was obtained in the dipole approximation, the excitations from a p level (for the L_2 and L_3 edges, for example) depend on the occupancy and, hence, on the magnetic properties of d states. Thus, the resonance $L_{2,3}$ scattering in 3d metals and their compounds provides information on the d bands. At the same time, in REM systems the $L_{2,3}$ scattering allows one to determine the magnetic properties of 5d bands in the dipole approximation, whereas the larger magnetic moments of 4f electrons manifest themselves only in the quadrupole approximation. The dipole and quadrupole contributions may be separated through their different dependence on the polarization and the wave vector [3].

(3) **Inelastic resonance scattering.** When $|i\rangle \neq |f\rangle$ in equation (12), a hole in the inner shell in the intermediate states $|n\rangle$ may be occupied by another electron, leaving a new hole in the valence band or in the inner shell, whereas the excited electron in the state $|n\rangle$ remains above the Fermi level. Thus, the final state $|f\rangle$ contains an excited electron – hole pair. Consequently, inelastic resonance scattering experiments reflect two-particle properties, much like optical absorption, differing, however, in the selection rules and the thickness of the material accessible for the investigation.

2.2 Comparison between neutron and X-ray magnetic scattering methods

Neutron scattering has been used for studies of magnetism for about 50 years, and in this period it has evolved into a powerful routine method for the determination of the magnetic structure of powders and single crystals, enabling one to study the spin dynamics of the process of inelastic scattering. X-ray magnetic scattering, which can provide more comprehensive information on magnetic structures, has found wide use slightly over 10 years ago. A comparison of the characteristics of these two methods is given in Table 1. To compare the possibilities of neutron and X-ray scattering, portions of diffraction patterns in the vicinity of the magnetic peak $(1,0,0)$ for $Mn_{0.75}Zn_{0.25}F_2$ are shown (Fig. 1). They were obtained for the same sample after its cooling to 30 K in an external magnetic field $H = 6$ T [16]. The $Mn_{0.75}Zn_{0.25}F_2$ system is an example of a three-dimensional disordered Ising model, whose phase diagram is determined by the competition of exchange interaction and frozen disorder. According to neutron scattering data, in the volume there exists a short-range order with a correlation length of about 80 nm. X-ray diffraction data obtained with better spatial resolution provide information on a surface layer about one micron in depth and are indicative of a long-range order in the surface layer.

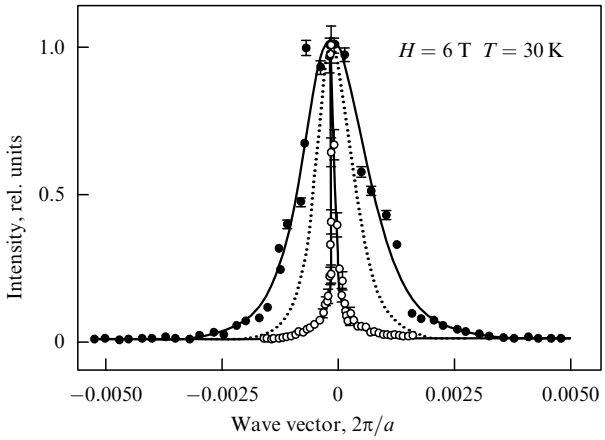

Figure 1. X-ray (open circles) and neutron (solid circles) scattering spectra in the vicinity of the magnetic satellite $(1,0,0)$ in $Mn_{0.75}Zn_{0.25}F_2$ obtained on the same sample. The wave vector is measured in units of the reciprocal lattice parameter $2\pi/a = 13$ nm^{-1} (from paper [16]).

2.3 Magnetic contribution to X-ray absorption

X-ray absorption spectroscopy (XAS) allows one to study electron transitions from inner atomic shells into unoccupied states. This method determines the volume properties of materials and provides unique information on the local electronic structure and the local distribution of atoms

Table 1. Comparison between the magnetic scattering methods for thermal neutrons and X-rays.

Neutrons	X-rays
De Broglie wavelength $\lambda \sim 0.03-2$ nm is of the order of the interatomic distances, so that diffraction provides direct information on the atomic and spin structures	Wavelength for SR is varied over a wide range, diffraction provides direct information on the atomic and spin structure
Energy $10^{-6}-1$ eV is of the order of the energy of the elementary excitations (phonons, magnons, and so on). Inelastic scattering provides information on these excitations and the atomic spin dynamics	Energy $1-10^3$ eV is too high to study the low-frequency dynamics (phonons, magnons)
Have no electrical charge, penetrate deep into the volume of a material. The small-angle scattering of neutrons can be used in studies of the surfaces of thin films and multilayer structures	Strongly interact with electrons. X-ray scattering exhibits better surface sensitivity in comparison with neutrons scattering. Soft X-rays with an energy below 4 eV penetrate the material a distance of only $10-10^3$ nm
Scattering length b_n depends on the nucleus, not on the atomic number Z directly. There exists an isotopic effect. The scattering length b_n does not depend on the scattering vector Q	X-ray charge scattering is determined by the atomic form factor $f_x(Q)$ depending monotonically on Z and approaching Z at $Q \to 0$. No isotopic effect. Very high resolution in the k space
Have the magnetic moment $\mu = 5.4 \times 10^{-4}\mu_B$ and interact directly with atomic/nuclear spins, providing information on the magnetic structure and dynamics	Have no magnetic moment, but the scattering amplitude depends on the densities of the spin and orbital moments in a material. It is possible to separate the spin and orbital contributions. Element-sensitive method in the vicinity of absorption edges.
Large samples are required (section ~ 1 cm^2).	Owing to the high intensity of SR and the resonance enhancement of a signal, it is possible to study small samples (~ 1 mm^2 for actinides)

around a given atom. The application of circularly polarized radiation provides a possibility for the study of the effects of magnetic circular dichroism in the absorption spectra of soft (XANES) and hard (EXAFS) X-rays. The MCD spectrum is defined as the difference of two photoelectron intensities measured for two opposite signs of circular polarization. The MCD method, being a differential one, provides a simple determination of the magnetic contribution to the spectrum (nonmagnetic contributions to these spectra are subtracted). Recall that X-ray spectra are specified by the term on which an X-ray hole is present; the correspondence between these two types of designations is as follows:

$$\begin{array}{cccccccccc} 1s_{1/2} & 2s_{1/2} & 2p_{1/2} & 2p_{3/2} & 3s_{1/2} & 3p_{1/2} & 3p_{3/2} & 3d_{3/2} & 3d_{5/2} \dots \\ K & L_1 & L_2 & L_3 & M_1 & M_2 & M_3 & M_4 & M_5 \dots \end{array}$$

Near the absorption edge, that is, in the energy range ~ 20 eV, large MCD effects are observed (in a number of cases more than 20% for relative values). At the present time the correct interpretation of experimental spectra is restricted to two limiting cases of electron behavior in the final state: localized states, which are described with the use of an atomistic approach (3d–4f transitions in REM systems, for example), and itinerant electrons, which are described by the band theory (1s–4p transitions in 3d elements and 2p–5d ones in 5d elements). For intermediate cases ($L_{2,3}$ spectra in 3d elements, for example), the kinetic energy of electrons is comparable to the potential energy on the order of magnitude, so that the effects of strong correlations are of importance. A complete theory of MCD for such systems is yet to be elaborated. For soft X-rays and band states, the absorption coefficient is described by Fermi's golden rule:

$$\mu_l(E) \sim \left|M(E)\right|^2 \rho_l(E)\,, \tag{13}$$

where $M(E)$ is the matrix element of a dipole transition, which is practically independent of the energy, and $\rho_l(E)$ is the density of unoccupied states with the projection l of the angular momentum in the vicinity of the Fermi level. If an absorbing atom (the elemental sensitivity is determined by the absorption-edge energy) has a spin magnetic moment, the final states will be split by the exchange interaction and the spin-up and spin-down densities of states will be different: $\rho_+(E_F) \neq \rho_-(E_F)$. The MCD signal

$$\mu_c = \frac{\mu_+ - \mu_-}{2} \sim \left|M(E)\right|^2 \left(\rho_+(E) - \rho_-(E)\right) \tag{14}$$

is proportional to the local spin density. Moreover, in Ref. [17] within the framework of the simple vector model of the addition of angular momenta, it is shown that the measurements of normalized MCD spectra near the L_2 and L_3 thresholds provide information both on the spin and orbital moments at once:

$$\frac{\mu_S}{\mu_B} \sim -\frac{4}{3}\int\left[\frac{\mu_c}{\mu_0}(E)\bigg|_{L_3} - \frac{\mu_c}{\mu_0}(E)\bigg|_{L_2}\right]\rho(E)\,dE\,, \tag{15}$$

$$\frac{\mu_L}{\mu_B} \sim -\frac{4}{9}\int\left[2\,\frac{\mu_c}{\mu_0}(E)\bigg|_{L_3} + \frac{\mu_c}{\mu_0}(E)\bigg|_{L_2}\right]\rho(E)\,dE\,. \tag{16}$$

Here, μ_0 is the absorption coefficient of unpolarized radiation.

For the localized final states of electrons, it is necessary to take into account the multiplet structure of the ionic terms, since many-electron effects make a contribution to this structure. In this case, too, sum rules [18] link the sum and the difference of MCD signals for two different initial inner shells with the local spin and orbital moments of partially filled valence states. Moreover, with the proviso that $\mu_0(L_3) = 2\mu_0(L_2)$, expressions (15) and (16) obtained in the band limit are equivalent to sum rules for the atomic limit [9].

In the region of hard X-ray absorption, there exists only a slight dependence of the EXAFS signal on the direction of circular polarization. The existence of contributions of spin-polarized EXAFS (SPEXAFS) in MCD is a commonly occurring phenomenon [19], however, the absence of any first-principles calculations of the signal hampers the extraction of quantitative information on local short-range order. Nevertheless, a comparative analysis of various systems shows the possibility of extracting information on the local short-range order [9].

2.4 Effects of strong electron correlations in X-ray absorption spectra

As was mentioned in Section 2.3, a rigorous interpretation of absorption spectra for narrow-bandgap materials, among these being many magnetic 3d-metal oxides, as well as REM and actinide compounds, requires taking into account strong electron correlations. For X-ray spectra, two types of correlations are important: first, correlations in the system of valence electrons; second, the correlations between valence electrons and an X-ray hole in the inner shell. We will consider the effects of correlations following the papers [20, 21].

We designate the Hamiltonian of the valence electrons as H_d, in which electron–electron interactions (Coulomb and exchange matrix elements) are explicitly included. These electrons do not have to be d electrons, they may be also f electrons for REM, while for oxides and other ionic compounds, the d and f states of a magnetic ion and the p states of an ion with hybridization and interaction effects are included in H_d. The interaction of the valence electrons with a hole in the inner shell is described by the Hamiltonian

$$H_{cd} = V_{cd} \sum_{\mathbf{r}\lambda\sigma\sigma'} d^+_{\mathbf{r}\lambda\sigma} d_{\mathbf{r}\lambda\sigma} n_{c\sigma'}\,. \tag{17}$$

Here, $d_{\mathbf{r}\lambda\sigma}$ is the annihilation operator of a valence electron in a unit cell with a radius vector $\mathbf{r}$ in an orbital state λ with spin σ, and $n_{c\sigma'}$ is the operator of the number of X-ray holes within the inner shell.

We assume that in a given unit cell, where a γ quantum is absorbed, there are N_e valence electrons. We designate the eigenfunctions of the Hamiltonian H_d as $\Psi^{(d)}_m(N_e)$, and the corresponding energies as $E^{(d)}_m$. The wave function of the cell in the initial state can then be written in the form

$$\Psi_i = \varphi^n_c \cdot \Psi^{(d)}_{0,i}\,, \tag{18}$$

where φ^n_c is the wave function of n electrons in the inner shells, $\Psi^{(d)}_{0,i}$ is the wave function of N_e valence electrons in the initial state calculated with consideration for strong correlations (for example, by way of the explicit diagonalization of a many-electron Hamiltonian H_d for a finite-size cluster representing the unit cell).

Within the sudden-perturbation approximation [22, 23], we have the operator of the number of holes in the inner shell $n_{c\sigma} \to 1$; then H_{cd} reduces to the shift of the valence electron levels in a crystal field. As a result, in the final state the function $\Psi^{(d)}_{m,f}$ of N_e valence electrons is calculated with the

Hamiltonian $H_d + H_{cd}$, and the total wave function of the final state can be written in the form

$$\Psi_f^{(m)} = \varphi_c^{n-1}\varphi_l \Psi_{m,f}^{(d)}(N_e)\,, \tag{19}$$

where φ_l is the wave function of a photoelectron with the energy ϵ_l in the state l. The energies of the initial and final states are

$$E_i = n\epsilon_c + E_{0,i}^{(d)}\,, \qquad E_{m,f} = (n-1)\epsilon_c + \epsilon_l + E_{m,f}^{(d)}, \tag{20}$$

respectively. The probability of absorption with the creation of a photoelectron is

$$I_m(\hbar\omega) = \left|\left\langle \Psi_i|e\mathbf{r}|\Psi_f^{(m)}\right\rangle\right| = \left|\left\langle \varphi_c(\epsilon_c)|e\mathbf{r}|\varphi_l(\epsilon_l)\right\rangle\right|^2 \times \left|\left\langle \Psi_{0,i}^{(d)}\left(E_{0,i}^{(d)}\right)\middle|\Psi_{m,f}^{(d)}\left(E_{m,f}^{(d)}\right)\right\rangle\right|^2. \tag{21}$$

If there was no interaction with the inner hole ($V_{cd} = 0$), the last factor in Eqn (21)

$$I^{(m)}(\Delta E_m) = \left|\left\langle \Psi_{0,i}^{(d)}\middle|\Psi_{m,f}^{(d)}\right\rangle\right|^2, \qquad \Delta E_m = E_{m,f} - E_{0,i}\,, \tag{22}$$

would be equal to $\delta_{m,0}$, and the spectrum would be determined by the one-electron matrix element

$$I_0(\hbar\omega_0) = \left|\left\langle \varphi_c|e\mathbf{r}|\varphi_l\right\rangle\right|^2, \qquad \hbar\omega_0 = \epsilon_l - \epsilon_c\,. \tag{23}$$

By this would be meant that the many-electron system of valence electrons is not involved in the process of absorption, which is determined by the one-electron transition $\varphi_c \to \varphi_l$. In fact, $V_{cd} \neq 0$, which results in the nonorthogonality of the initial and final states of valence electrons. Taking into account that the energy of the absorbed γ photon is

$$\hbar\omega = E_{m,f} - E_i = \hbar\omega_0 + \Delta E_m \tag{24}$$

and summing over all final states, we obtain the following expression for the absorption spectrum with the creation of a photoelectron:

$$I(\hbar\omega) = \sum_m I_0(\hbar\omega - \Delta E_m) I^{(m)}(\Delta E_m)\,. \tag{25}$$

This expression implies that the spectrum with consideration for correlations is described by the convolution of two spectra: the spectrum of one-electron transitions I_0, but with a shift in energy ΔE_m, and the discrete spectrum of satellites $I^{(m)}$ determined by the nonorthogonality of the different final states of valence electrons, on the one hand, and the ground state, on the other.

In a similar manner, the white line in the $L_{2,3}$ absorption spectrum can be considered. In this case, the final state can be written in the form

$$\Psi_f^{(m)} = \varphi_c^{n-1}\Psi_{m,f}^{(d)}(N_e + 1)\,,$$
$$E_{m,f} = (n-1)\epsilon_c + E_{m,f}^{(d)}(N_e + 1)\,. \tag{26}$$

For the absorption spectrum, we obtain the same formula (26), where I_0 is now determined by the one-electron matrix element $\varphi_c \to \varphi_d$, and

$$I^{(m)}(\Delta E_m) = \left|\left\langle \Psi_{0,i}^{(d)}(N_e)|d_{\mathbf{r}\lambda\sigma}|\Psi_{m,f}^{(d)}(N_e + 1)\right\rangle\right|^2. \tag{27}$$

This quantity can be also calculated if the many-electron states $\Psi_{m,f}^{(d)}$ are obtained for each sector of the Hilbert space with its own number of valence electrons N_e. In the concrete calculations of the Cu K spectra and Cu $L_{2,3}$ spectra of La_2CuO_4 [20, 21], the quantity $I^{(m)}$ was found by way of explicit diagonalization of the multiband p–d model Hamiltonian for a CuO_4 cluster. In particular, a high-energy satellite (C peak) in the Cu K spectra shifted in energy by 7.8 eV from the main peak was obtained in accordance with experiments [24].

3. Experimental methods for the study of magnetic properties based on the use of synchrotron radiation

Synchrotron radiation occurs when high-energy charged particles (electrons and positrons) move in a magnetic field following a curved trajectory. It has long been used in high-energy physics, solid-state physics, chemistry, and biology. The fundamental properties of SR as well as methods of its production, relevant equipment, and the description of possible applications were presented in the reviews [25–27]. The third generation of present-day SR sources is based on storage rings and characterized by a high intensity and a high degree of polarization. A typical photon flux exceeds 10^{12} photon/s in a spot of area 1 mm^2 in an energy bandwidth of 5 mV. In present-day sources, synchrotron radiation is produced with the use of undulators or wigglers, which provide a higher intensity than the usual bending magnets [28–30]. At the present time, SR sources of the fourth generation are being discussed; their brilliance will be 2–3 orders of magnitude greater [37].

No less than ten large-scale modern centers of research into materials science using SR can be counted in the world. The biggest SR centers are ESRF, Grenoble, France; Argonne National Laboratory, USA; and Spring-8, Japan. Big SR centers are also in Brookhaven, USA, and in France (LURE). Other centers, such as Hasylab, Hamburg; BESSY, Berlin; Photon Factory in Tsukuba, Japan, are also worthy of note. And there are many beamlines for various investigations in each center.

In LURE, for example, five SR beamlines are dedicated to research into magnetic materials; more than 50% of the works of the Solid State Physics Division and about 20% of the works of Surface Physics and Chemistry Divisions are devoted to magnetism [54]. The SU22 beamline operates in the range of 800–2000 eV with resolution $\Delta E/E \approx 4 \times 10^{-4}$ at $E = 1$ keV. The SU23 beamline is dedicated to experiments with the use of soft X-rays in the range of 100–1000 eV with resolution $\Delta E/E \approx 3 \times 10^{-4}$ at $E = 700$ eV. The SU23 beamline is directly attached to a chamber for molecular-beam epitaxy equipped with low-energy and high-energy electron diffractometers and an Auger spectrometer used mainly for the investigation of the magnetic properties of thin surface layers and interfaces. An asymmetric wiggler serves as the source of SR for the SU22 and SU23 beamlines. A bending magnet is used for producing SR in the SU7 beamline, operating only with linearly polarized X-rays.

Most investigations of magnetic materials in LURE concern resonance magnetic scattering and MCD methods. There are possibilities to study MCD spectra under pressure and in high magnetic fields. In addition, time-resolved magnetometry and the element-sensitive magnetometry based on the MCD method are used [54].

In the European Center, ESRF, Grenoble, X-ray radiation is produced by third-generation SR sources. Three beamlines — ID12A, ID12B and ID20 — are fully devoted to magnetic research, and four more — ID3, ID10, ID15 and ID24 — are partially operated with magnetic materials as well. The following methods are used: nonresonance magnetic diffraction (enabling one to separate the orbital and spin parts in the magnetic form factor), resonance magnetic scattering (providing element-sensitive information for very thin films), time- and spatial-resolved MCD. Examples of concrete investigations are presented in the following section.

In Russia, the main center of the application of synchrotron radiation to the problems of materials science is G I Budker Institute of Nuclear Physics in Novosibirsk (INP SD RAS: Institute of Nuclear Physics, Siberian Division, Russian Academy of Sciences). In the near future, after putting into operation a Siberia-2 SR facility, investigations with the use of SR in the Kurchatov Institute Russian Research Center are planned.

We consider in more detail the experimental possibilities of the Siberian Center of synchrotron radiation at the INP SD RAS. At the present time, three storage rings are used as sources of SR: VEPP-2M, VEPP-3 and VEPP-3M. All synchrotron radiation stations operating with these storage rings are listed in Table 2 [38, 39]. The VEPP-2M electron–positron storage ring is used in the range of ultraviolet radiation and soft X-rays ($\lambda = 5 \times 10^2 - 0.2$ nm). The VEPP-3 is the main source of SR in the X-ray region. In 1996, a wiggler servicing eleven beamlines and generating radiation in the range of $0.1 - 1$ nm was put into operation on the VEPP-3 storage ring. As a rule, research into new materials is conducted on the VEPP-3 storage ring. Among recent papers are those concerning the investigations of magnetic alloys $Cu_{30}Cr_{70}$ [40] and $Co_{16}Pd_{84}$ [41] and multilayer Co/Pd structures [42, 43]. The first experiments on studies of the periodic structures of nanowires in multilayer Ni/Cu matrices have been carried out [39].

The investigations of magnetic materials can be subdivided into SR scattering and SR absorption experiments with the use of both the linear and circular polarization of photons. For practical applications, thin films fabricated in ultrahigh vacuum are of interest. These objects must be studied *in situ*; therefore, modern setups are equipped with special vacuum chambers for the preparation and investigation of such thin-film samples.

At the present time, X-ray diffraction has evolved into the most powerful method for the investigation of the structure of thin films and multilayers which provides high resolution in the k space. A standard present-day three-axis diffractometer is equipped with high-quality single crystals (usually Ge or Si)

Table 2. Beamlines and experimental stations of the VEPP-2M, VEPP-3 and VEPP-3M storage rings.

SR beamline	Synchrotron radiation facility	Experimental station
VEPP-2M		
1E	wiggler	not used
2E	wiggler	not used
3E	bending magnet	photoelectron spectroscopy for chemical analysis
4E	bending magnet	not used
1P	bending magnet	not used
2P	bending magnet	time-resolved luminescence
3P1	bending magnet	metrology (soft X-rays)
3P2	bending magnet	VUV (vacuum ultraviolet) spectroscopy
4P	bending magnet	stimulated gas photodesorption 1
5P	wiggler	measurements of positron-beam parameters
6P	bending magnet	stimulated gas photodesorption 2
VEPP-3		
2	wiggler	high-resolution X-ray diffraction and anomalous scattering
3	wiggler	X-ray fluorescence analysis
4	wiggler	angiography
5	wiggler	(a) X-ray microscopy and microtopography; (b) time-resolved diffractometry; (c) macromolecular crystallography; (d) inelastic scattering; (e) small-angle scattering
6	wiggler	time-resolved spectroscopy
7	wiggler	LIGA, X-ray topography and diffractometry
8	wiggler	EXAFS spectroscopy
10	bending magnet	X-ray lithography
VEPP-4M		
1	bending magnet (0.8 T)	EXAFS
2	bending magnet (1.3 T)	EXAFS
3	bending magnet (1.3 T)	diffraction movies
4	bending magnet (1.3 T)	elemental analysis
5	bending magnet (0.9 T)	small-angle scattering
6	bending magnet (0.9 T)	anomalous scattering
7	bending magnet (1.3 T)	diffractometry
8a	wiggler	medicine
8b	wiggler	microscopy
9	bending magnet (1.35 T)	inelastic processes
10	bending magnet (1.35 T)	metrology
12	bending magnet (0.95 T)	LIGA
13	bending magnet (1.35 T)	reserved
14	bending magnet (1.35 T)	technical beamline

serving as a monochromator and analyzer. A typical present-day resolution for the wavevector transfer approximates 0.002 nm or higher, which enables one to study the peculiarities in photon scattering determined by correlations in a structure with characteristic scales from 1 to 10^3 nm. The analysis of the polarization dependences of the scattering cross section in the nonresonance case [Eqn (8)] allows one to determine the Fourier transforms of the orbital and spin magnetic moments individually.

In the resonance mode of X-ray scattering, the energy of incident photons is varied in the vicinity of an absorption edge. The strongest effects of the resonance enhancement of the scattering cross section are observed near the L and M edges. For REM, the L absorption edge is easily accessible in the vicinity of energies of about 8 keV. In actinides, the M absorption edge lies in the vicinity of 3.7 keV, which allows one to conduct diffraction experiments. For transition elements, the L edge lies below 1 keV. The strong resonance enhancement of the magnetic scattering of photons enabled one to study magnetic structures for a broader class of materials than was expected after the first experiments on monatomic substances [2]. More recently, the possibility of investigating alloys [31, 32], magnetic superlattices [33], and surfaces [34, 35] was demonstrated.

The spectra of magnetic circular dichroism can be studied in different ways (Fig. 2). X-ray absorption spectra (XAS) can be obtained by measuring the transmitted or reflected flux of γ photons or determined indirectly from measurements of the decay rate for a hole created in the inner shell. In the last case, both fluorescence and photoemission spectra can be measured. The total photoemission yield is determined from the value of the photocurrent, and the partial ones — with the use of an electron-energy analyzer. Different methods gather information from different depths: fluorescence spectra are formed in layers of $\sim$100 nm in thickness and provide information on volume properties, whereas photoelectron spectra are determined by the electron escape depth (no more than 10 nm) and are surface-sensitive.

The spectrum of MCD is the difference of absorption spectra for two opposite directions of the angular momentum of a photon: parallel and antiparallel to the electron spin. Instead of changing the direction of polarization, in practice the method of reversing the magnetization of a sample by inverting the direction of the magnetic field has turned out to be more convenient. MCD spectra for magnetic materials were first obtained in the hard X-ray range (EXAFS) [19] and then in the range of soft (XANES) photons [36].

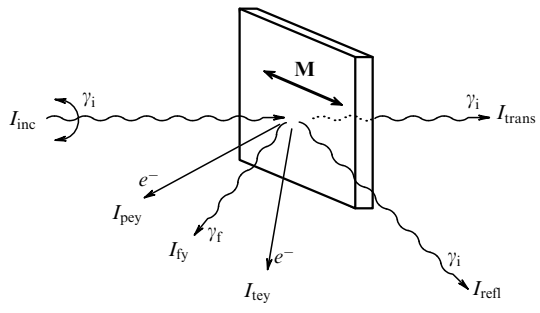

Figure 2. Geometry of five different methods for investigation of the spectra of magnetic circular dichroism in a sample with magnetization **M**. The incident beam I_{inc} can be used for normalization of the transmitted beam I_{trans}, the reflected beam I_{refl}, the total yield of electrons I_{tey}, the partial yield of fluorescence I_{fy}, and the partial yield of electrons I_{pey} (from Ref. [71]).

4. Examples of investigations of magnetic materials

It is not the aim of this review to give a comprehensive description of the magnetic and electron properties of concrete materials using various available data. The results discussed below rather demonstrate the most likely possibilities of X-ray magnetooptics as a tool for the study of the different characteristics of magnetic materials.

4.1 Magnetic circular dichroism in 3d metals

It was found, using a simple atomic-like model [44], that the ratio of the intensities of the X-ray L_3/L_2 MCD spectra is equal to -1. The first measurements for Ni have revealed a considerable deviation from -1 [45]. As was shown in Ref. [46], this distinction is caused by the spin – orbit interaction. For the $L_{2,3}$ spectra, which are determined by the p – d transitions of electrons, the following sum rules linking MCD spectra with $\langle L_z \rangle$ and $\langle S_z \rangle$ were obtained [18]:

$$\frac{\langle L_z \rangle}{\langle S_z \rangle} = \frac{4}{3}\,\frac{R_M + 1}{R_M - 2}\,, \tag{28}$$

where $R_M = I(L_3)/I(L_2)$ is the ratio of the integrated intensities of the appropriate MCD signals. MCD spectra for all 3d metals are presented in Fig. 3 [47]. The samples were magnetized *in situ* by a field of 0.2 T. To obtain the signal of dichroism, reversing the magnetic field at a fixed polarization of photons was used. The following samples were used: a multilayer V/Fe structure, and submonolayer films of Cr on Fe, Mn on Co and Fe, Co and Ni on Cu(001). The splitting of the L_2 and L_3 peaks decreases monotonically when moving from Ni to V; for V and Cr, there is no clear separations of the peaks. The high-energy satellite B in the L_3 spectrum of Ni and Co is determined by the mixing of configurations with different multiplicities in the initial state, for example, d^9 and d^8 for Ni [48]. The second arrow in Fig. 3 points to a low negative intensity in a region between the satellite B and the L_2 peak in Ni and Co. The authors of paper [47] associate this intensity with the diffuse magnetic moments that were found in Fe, Co and Ni with the use of diffraction of polarized neutrons [49]. According to band calculations [50], these moments are determined by the sp electrons whose spins are polarized in opposition to the spins of 3d electrons. The magnitude of the diffuse moments comprises less than 10% of the total moment magnitude (0.21, 0.28 and 0.105, according to neutron data [49], and 0.04, 0.07, and 0.04 μ_B, according to calculations [50], for Ni, Co and Ni, respectively).

The ratios of the orbital and spin moments calculated from the sum rule (28) are listed in Table 3. Since only the p – d transitions were taken into account when deriving the sum rule, the presence of moments in 4s states results in a systematic error in the determination of $\langle L_z \rangle$ and $\langle S_z \rangle$, since dipole 2p – 4s transitions are permissible and make a contribution to the MCD signal. The corrections for diffuse moments are taken into account in values listed in the second line of the table. These corrections result in decreasing the ratio $\langle L_z \rangle / \langle S_z \rangle$ and approaching the values following from the neutron data [49] and the band calculations [51].

A similar MCD spectrum for the $L_{2,3}$ absorption in Fe films was obtained in work [9]. For two samples of different

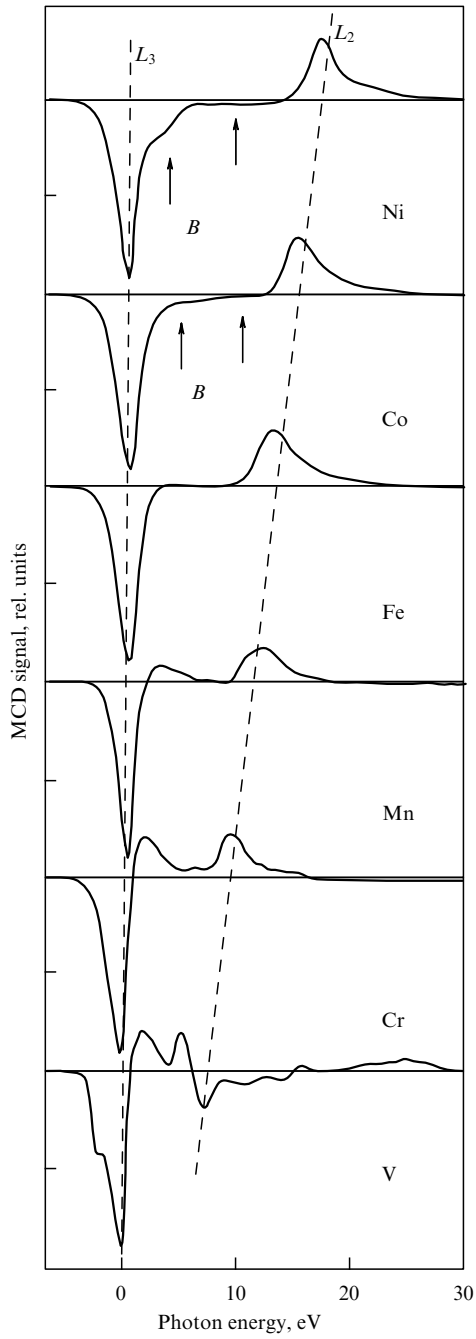

Figure 3. X-ray $L_{2,3}$ spectra of MCD for V, Cr, Mn, Fe, Co and Ni normalized to the constant height of the L_3 peak (from paper [47]).

thicknesses, 0.925 and 2.4 nm, the use of the sum rule under the assumption that the number of holes n in the d shell is equal to 4 gave the following values of the spin and orbital moments: $m_S = 2.19\mu_B$, $m_L = 0.25\mu_B$ and $m_S = 2.29\mu_B$, $m_L = 0.21\mu_B$, respectively. The m_L/m_S ratio averaged over these two samples [9] is presented in the third row of Table 3. Using data on MCD [59], the authors of paper [18] obtained with the help of the sum rule (28) their own values of the $\langle L_z\rangle/\langle S_z\rangle$ ratio, which are also listed in the table. It is seen that the conclusions of different authors are similar in a qualitative sense, although their quantitative results are different.

Another impressive example of the $L_{2,3}$ spectra of MCD was demonstrated in studies of the impurities of 5d elements in iron. In this case, the largest signal was observed at an

Table 3. $\langle L_z\rangle/\langle S_z\rangle$ ratio obtained by the X-ray MCD and neutron diffraction methods along with the band-calculation data.

Method	Ni	Co	Fe	Mn	Cr
MCD [47]	0.39	0.33	0.17	0.25	0.065 ± 0.02
MCD without diffuse moments	0.28	0.25			
MCD [9]			0.10		
MCD [18]	0.19	0.13	0.13		
Theory [51]	0.22	0.15	0.08		
Neutron diffraction [49]	0.17	0.14	0.12		

impurity concentration of 3 at.% [52]. Good agreement with the theoretical calculations of MCD spectra was obtained for the following impurities: Hf, W, Re, Os, Ir, Pt and Au. The values of the local magnetic moments of the 5d-element impurities are shown in Fig. 4. From this figure, good agreement with the neutron data [53] is also seen.

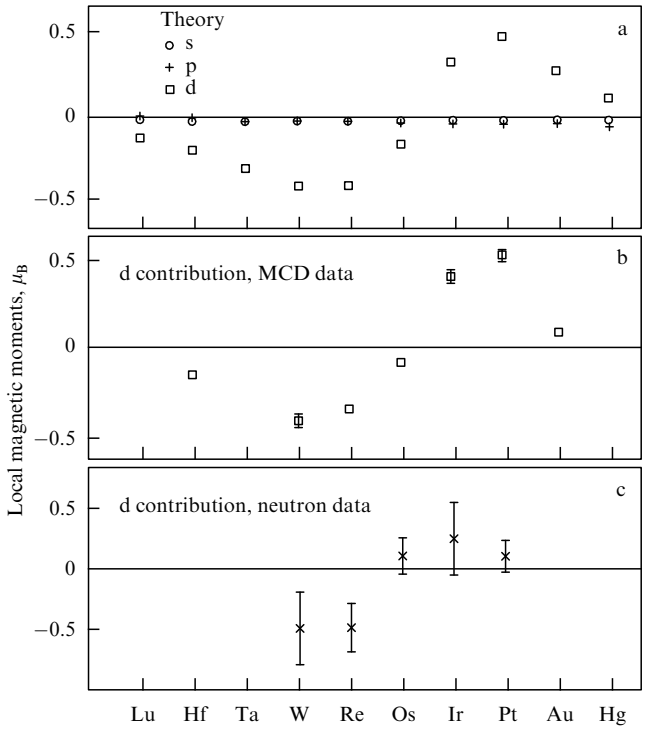

Figure 4. Local magnetic moments of the impurities of 5d elements in iron: (a) one-electron calculations; (b) the contribution of d electrons from MCD spectra; (c) neutron data [53] (from paper [52]).

Interesting possibilities are provided by the combination of MCD and high pressure. The results of the investigation of MCD in the vicinity of the L_3 edge of Pt in $PtFe_3$ are shown in Fig. 5. The existence of MCD for the L_3 signal in Pt points to the spin polarization of the 5d electrons of Pt in the molecular field of Fe. This polarization sharply decreases on going from the high-spin state to the low-spin state of Fe at a pressure of about 4 GPa, then (up to a pressure of 13 GPa) the signal varies only slightly, and at $p > 20$ GPa the MCD effect dies out, which is indicative of going to a nonmagnetic state [54]. This experiment is the first explicit proof of the existence of a nonmagnetic state of $PtFe_3$ at high pressures. Such experiments are extremely complicated, since the intensity of the MCD signal is inevitably decreased because of absorption in the diamond anvil used for creating pressure. Therefore, for

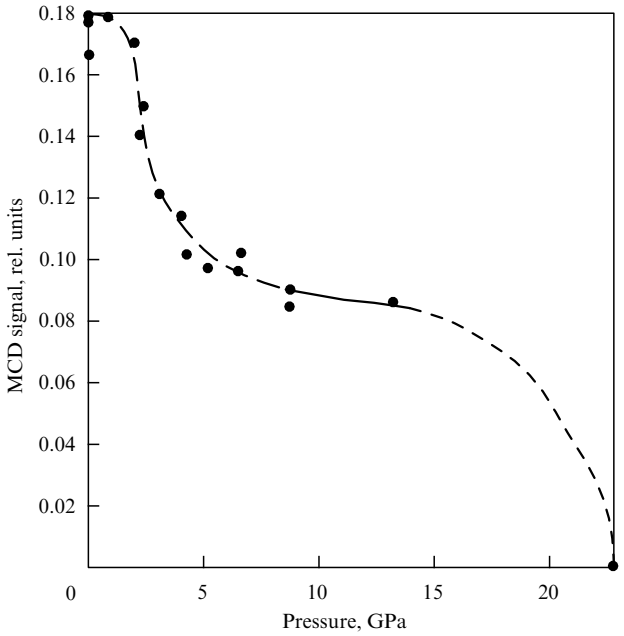

Figure 5. Pressure dependence of the MCD signal for the L_3 edge of Pt in $PtFe_3$ [54].

the further development of such experiments under pressure it is necessary to increase the intensity of the synchrotron radiation source.

The high spatial resolution of the X-ray magnetic scattering method was used for the study of incommensurate spin-density waves (SDW) and charge density waves (CDW) in Cr [55]. These are periodic structures for which the ratio of the period of the structure to the period of the lattice is expressed by an irrational number. In reciprocal space, the period of the wave is determined by the vector $Q = (1 \pm \delta)2\pi/a$. In Cr, below $T_N = 311$ K there exists an incommensurate SDW with a modulation period $\sim 27a$; the incommensurability parameter δ below T_N approximates 0.037 and increases up to ≈ 0.048 at $T = 10$ K. The lattice distortion has the form of a CDW and was found earlier by the neutron diffraction method. These neutronographic data were substantiated in Ref. [55]. In addition, measurements of the higher harmonics of CDW and SDW have shown that these waves are not described by simple sinusoids.

4.2 Rare earth metals and their compounds

Complex magnetic structures with cascades of phase transitions between them are typical of heavy REM. Among these structures, ferromagnetic, helicoidal, conical structures, and incommensurate spin density waves are worthy of note [56, 57]. For Ho single crystals, in particular, the magnetic structure was studied by the neutron diffraction method [58]. These single crystals are characterized by an incommensurate helicoidal structure in the temperature range $T_C = 20\ \text{K} < T < T_N = 132\ \text{K}$; below T_C, a ferromagnetic component along the c axis arises. The presence of the incommensurate magnetic structure manifests itself in neutron diffraction patterns in the form of additional lines (satellites), for example, $(1, 0, -q)$ and $(1, 0, +q)$ near the composite peak $(1, 0, 0)$, where q is the modulation vector of the magnetic structure. As the temperature decreases below T_N, the vector q smoothly varies from $q = 50/\pi$ to $q = 1/6$; the latter value corresponds to the commensurate phase existing below T_C.

Magnetic X-ray diffraction provides the same information [59], in particular, satellites for Ho are observed, which indicate the presence of an incommensurate magnetic structure. Figure 6 illustrates the $(0, 0, 2 + q)$ satellite obtained by the resonance scattering method near the L_3 absorption edge [60]. X-ray diffraction provides better angular resolution than neutron diffraction, and this is of great importance in studies of incommensurate structures. The temperature dependences of the sublattice magnetization and the modulation vector q are close to the neutron diffraction data. The amplitude of the resonance SR scattering exhibits a sharp maximum near the L_3 absorption edge. There are no analogies to this effect in magnetic neutron scattering. This maximum is determined by a pure atomistic effect specific of a given element, which allows one to measure magnetic moments, for example, in complex compounds, for each element individually. The high precision of resonance X-ray scattering enabled one to determine the critical indices of the formation of incommensurate structures in the neighborhood of the Néel point in Dy, Ho, Er and Tm [61]. It was found that for Er and Tu the index of the order parameter is close to the mean-field value: $\beta(\text{Er}) = 0.47 \pm 0.05$, $\beta(\text{Tm}) = 0.49 \pm 0.06$, whereas for Dy $\beta = 0.36 \pm 0.04$ and for Ho $\beta = 0.41 \pm 0.04$. These values are close to the value $\beta = 0.39$ resulting from the symmetric $O(4)$ model [62].

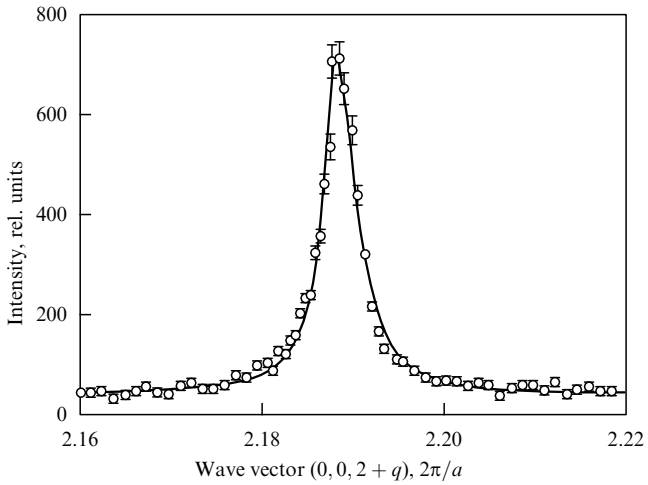

Figure 6. Magnetic satellite $(0, 0, 2 + q)$ in Ho at $T = 30$ K obtained at resonance X-ray scattering near the L_3 edge [60].

The spin and orbital contributions to the magnetic moment of Ho were determined by the measurement of the degree of linear polarization for nonresonance scattering [59]. Fig. 7 illustrates three possible alternatives: a pure spin contribution ($L = 0$), a pure orbital contribution ($S = 0$) and the state $S = 2$, $L = 6$ corresponding to Hund's rule for Ho^{3+}. It is seen that only the last alternative is consistent with the experiment.

The contributions of dipole and quadrupole transitions can be separated with the use of inelastic scattering. For example, if a $2p_{3/2}$ hole is created near the L_3 edge of an REM, the excited electron may occur in the 5d band as the result of a dipole transition or at the 4f level as the result of a quadrupole transition. The intermediate states may decay when a 3d electron goes to the 2p shell, so that for the initial $4f^n5d^m$ state

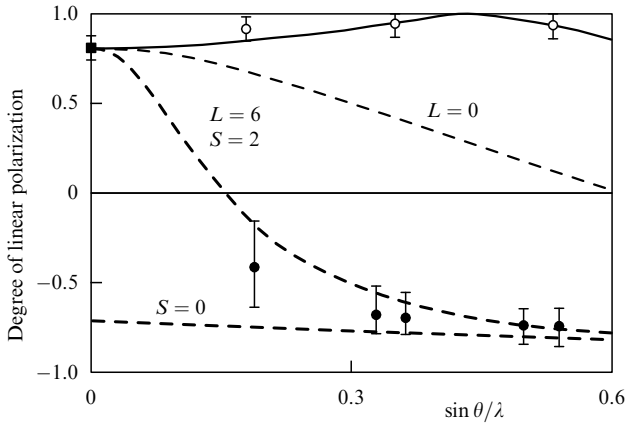

Figure 7. Wave-vector dependence of the degree of linear polarization for nonresonance X-ray scattering in Ho [59]. The open circles correspond to charge scattering; the solid circles, to a magnetic satellite.

two configurations of the final states are possible: $3d^9 4f^{n+1} 5d^m$ or $3d^9 4f^n 5d^{m+1}$. Owing to strong electron correlations, the energies of the three terms are different. For example, in the case of Gd with the initial state $4f^7 5d^0$, the multiplets of the final states $3d^9 4f^8 5d^0$ and $3d^9 4f^7 5d^1$ are separated by 8 eV [63], so that the features in the absorption spectrum at an energy of 7240 eV correspond to a quadrupole transition to the configuration $2p^5 4f^8$, whereas those located at 7247.5 eV are associated with a dipole transition to the configuration $2p^5 5d^1$.

Near the L absorption edge in REMs with characteristic photon energies of 5–10 keV, well-marked MCD signals [17, 19] are observed (for example, for the overall series of R_2Co_{17}). For Gd in metallic state, in ferromagnetic oxides, and in binary compounds, the MCD signal is proportional to the polarization of photoelectrons calculated for a free atom. The same situation exists for Ce in Ce_2Co_{17} and $CeFe_2$. At the same time, the calculation of the polarization of 5d electrons in the framework of the one-electron theory ($\mu_d^{(theor)} = +0.4\mu_B$) is in contradiction with experimental data on MCD ($\mu_d^{(exp)} = -0.25\mu_B$) [52]. In ferrimagnets, the elemental sensitivity of the MCD method allows one to determine the temperature dependences of the magnetic moments of individual sublattices, which was made for $Gd_3Fe_5O_{12}$ [64] (near the L_3 absorption edge). The spin-dependent EXAFS method provides additional information on the magnetic short-range order. The SPEXAFS signal for $Eu_3Fe_5O_{12}$ is shown in Fig. 8. On the top of this figure, absorption spectra with the L_2 and L_3 edges of Eu and K edge of Fe are shown, at the center the SPEXAFS signals χ_c for the L_2 and L_3 edges of Eu along with a small contribution from the K edge of Fe are presented. The Fourier transforms of the EXAFS signals χ_0 (charge scattering) and SPEXAFS signals (magnetic scattering) are shown at the bottom of the figure. It is seen that the main peak in the EXAFS spectra associated with the nearest neighbors — oxygen atoms — is not present in the SPEXAFS spectra, where the main peak corresponds to the position of the four nearest magnetic neighbors — iron atoms. Weaker magnetic peaks correspond to the next coordination shells involving 16 atoms of Fe and 8 atoms of Eu.

Magnetic phase transitions in amorphous alloys $Fe_{73}Er_{27}$ were investigated by the MCD method in Ref. [65]. The Fe and Er lattices ordered antiparallel in this magnet are noncollinear; there exists a so-called asperomagnetic structure, which is characterized by a fanlike orientation of magnetic moments in each sublattice. When changing the temperature or magnetic field, spin-reorientation transitions with reversal of the sublattice magnetization are possible. In Fig. 9, the signals of MCD for the M_5 edge of Er determined by the dipole 3d–4f transitions are shown. The temperature dependence was measured in the field $H = 1$ T, and the field dependence was obtained at $T = 25$ K. A negative MCD signal at $T = 4$ K points to the fact that the magnetization of Er is parallel to the external field. At $T = 15$ K the system is close to the compensation point and the MCD signal is small. Above the compensation point, the signal changes its sign and the magnetization of Er becomes antiparallel to the external field. A decrease in the signal with a further increase of T is connected with approaching the ordering temperature. The largest moment of Er at $T = 50$ K approximates $3\mu_B$, which is much less than at saturation ($\mu = 9\mu_B$). This means that the opening of the magnetic moment fan of the Er sublattice is considerable and thus the existence of an asperomagnetic structure in this alloy is confirmed. The field dependence of the MCD signal shows the existence of two points of compensation at $T = 25$ K: in a low field $H = 0.2$ T and in the field $H = 3-4$ T. This is indicative of a marked curvature of phase transition lines in the (H, T) phase diagram.

4.3 Actinides

X-ray resonance magnetic scattering (XRMS) manifests itself most clearly in actinides. In UAs, the amplitude of the antiferromagnetic Bragg peak in the vicinity of the M_4 absorption edge increases by a factor of 10^7, with the result that the intensity of the XRMS signal amounts to 1% of the value of the charge scattering signal [66]. Similar effects were also found in other uranium compounds, such as UN and UO_2 [67]. For the compound URu_2Si_2, the magnetic moment ($0.04\mu_B$) and its temperature dependence were measured.

An example of determination of the fine details of a magnetic structure is the application of the XRMS method to UX compounds. As is known, UTe is a ferromagnet and USb is an antiferromagnet. In $USb_{1-x}Te_x$ solid solutions at $x \leqslant 0.2$ there appears an incommensurate phase. For example, at $x = 0.2$ this phase exists in the temperature range $160\ \text{K} < T < 200\ \text{K}$; the magnetic moments of uranium are aligned along one of the directions $[1, 1, 1]$ with the modulation vector $(0, 0, q)$ [68].

Using the neutron diffraction method, it was shown that below $T_N = 206$ K there appears a satellite with $q \approx 0.4$ and, as the temperature decreases, a second modulation arises with $q \approx 0.2$, becoming dominant at $T = 165$ K [69]. In the same work, it was shown that the XRMS method allows one to study the satellite $(0, 0, 2 + q)$ with a better spatial resolution than in the case of neutron diffraction, and several incommensurate structures in the temperature range of 165–190 K were found. Of prime importance is the high spatial resolution in studies of fluctuations in the neighborhood of the phase transition points, which allows one to determine the inverse correlation length x from the Lorentz-line width in the spectrum. For $USb_{0.8}Te_{0.2}$, the line shape obtained using neutrons and XRMS is close to the Lorentz-line shape and the x values determined by both methods are the same [69]. However, the XRMS method not infrequently produces signals of more complex shapes. For example, in USb the signal is described by a combination of the usual Lorentz curve and a sharper function that corresponds to the Lorentz

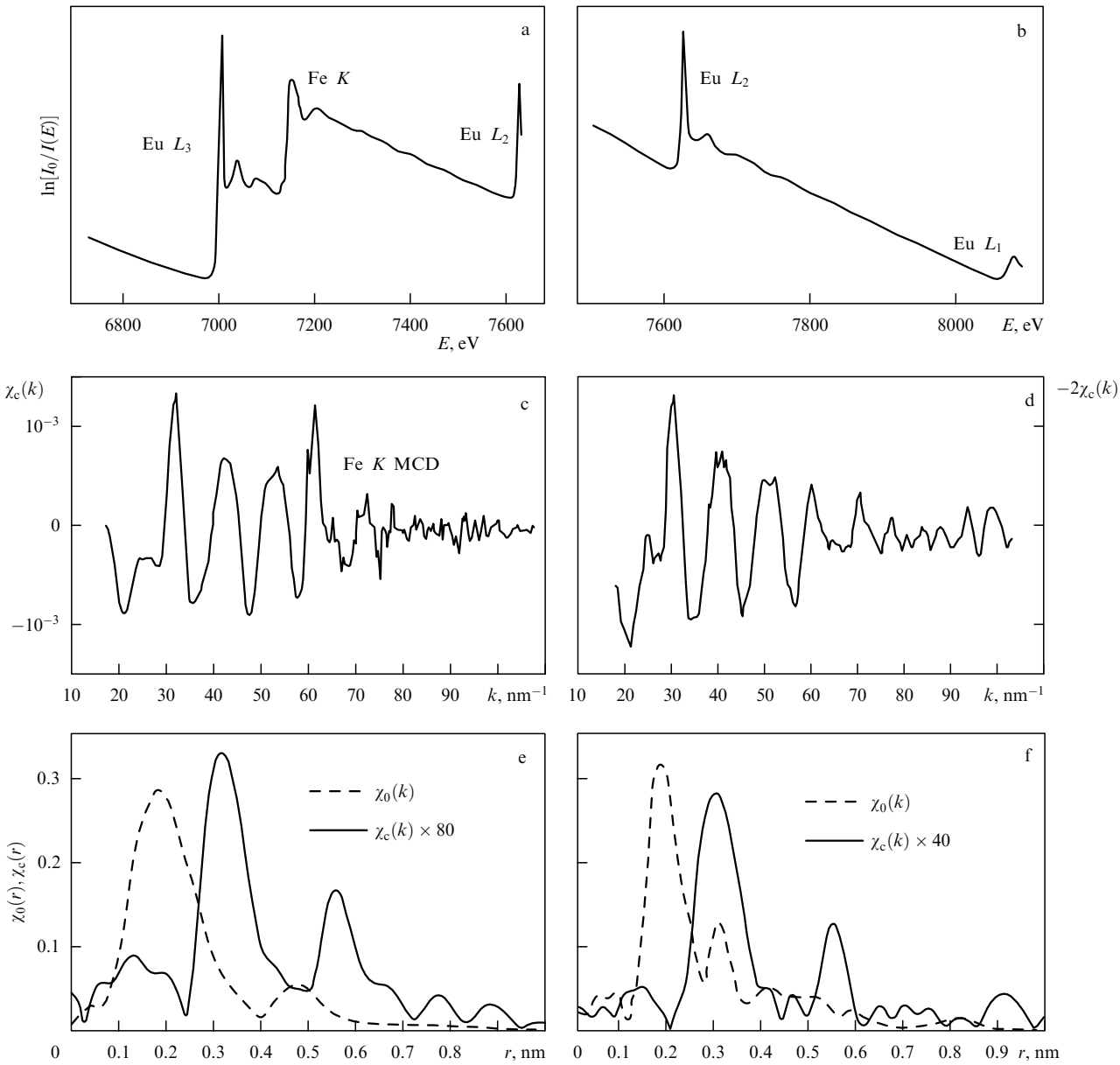

Figure 8. Absorption spectrum of $Eu_3Fe_5O_{12}$ in the range of 6700 – 7680 eV (a) and 7480 – 8120 eV (b); SPEXAFS for L_3 (c) and L_2 (d); at the bottom of the figure, the Fourier transforms of the EXAFS (dotted line) and SPEXAFS (solid line) signals for the L_3 (e) and L_2 (f) edges are given [9].

function squared [70]. The explanation of such a two-component critical scattering remains unknown to us. The separation of spin and orbital contributions in an antiferromagnetic UAs was performed with the use of nonresonance magnetic scattering [71]. An analysis of the photon polarization has shown that the orbital magnetic moment makes a dominant contribution to the total magnetic moment and that the L/S ratio is close to its value for a free $5f^3$ ion.

The high intensity of the XRMS signal in actinides ($\sim 10^6$ counts per second) allows one to conduct investigations of small crystals (with an area of ~ 0.2 mm^2 and mass less than 1 mg), which provides a number of advantages as compared to neutron investigations. First, the smaller single crystals are more perfect; second, small radioactive samples are simpler to handle; third, it is possible to study the magnetic properties of materials such as curium, berkelium, californium and other transuranic elements, which usually cannot be studied by the standard methods of solid-state physics.

4.4 Thin films and multilayer structures

For multilayer structures with different magnetic layers, the elemental sensitivity of the MCD method allows one to obtain information from each individual layer, which is impossible with magnetic neutronography. Thus, for example, for the Cu(4 nm)/Co(5.1 nm)/Cu(3 nm)/Fe(10.2 nm) structure, hysteresis loops were measured individually for the Co layer and the Fe layer using the MCD method (Fig. 10). MCD signals for the Co L_3 and Fe L_3 absorption edges were measured as a function of the external magnetic field [71]. The sum of hysteresis loops of individual layers was practically indistinguishable from the loop measured by a vibration-sample magnetometer for the whole sample. The distinction between magnetization-reversal processes for different layers was also investigated by the XRMS method [71]. The results of static measurements with the use of a vibration-sample magnetometer and the XRMS signal for the sandwich structure NiFe(5 nm)/Cu(3 nm)/Co(2nm) are

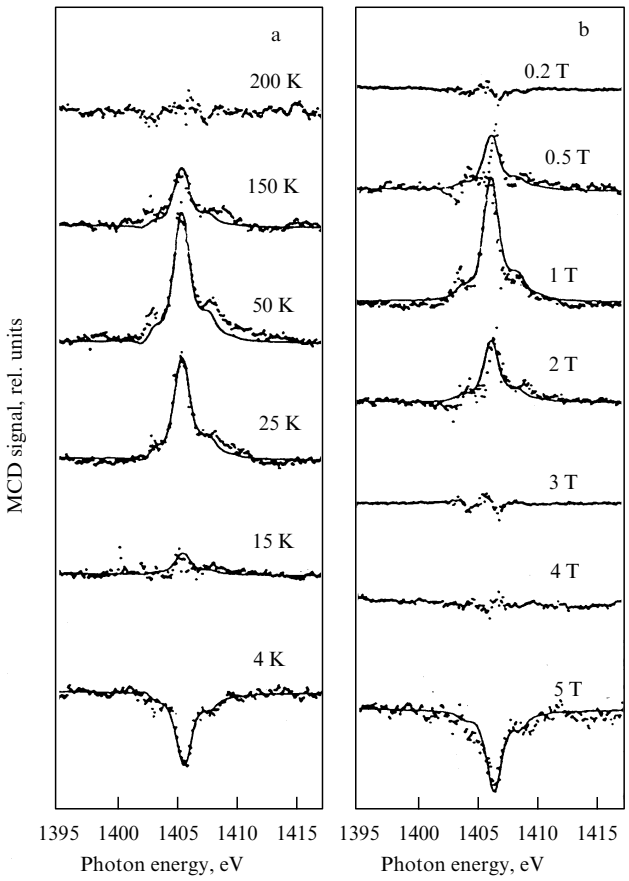

Figure 9. Temperature (a) and magnetic-field (b) dependence of the MCD signal near the M_5 edge of Er in an amorphous alloy $Fe_{73}Er_{27}$ [65].

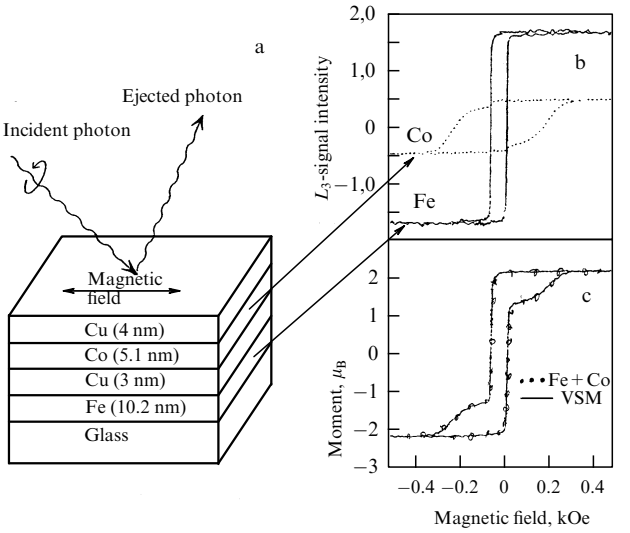

Figure 10. Scheme of the element-sensitive layer-by-layer magnetometry for a Cu/Co/Cu/Fe structure on a glass substrate (a). On the right, hysteresis loops for Fe (solid line) and Co (dashed line) layers (b) and a hysteresis loop for the whole sample measured by a vibration-sample magnetometer (VM) (c) are shown (the points on the curve correspond to the sum of the signals for Fe and Co).

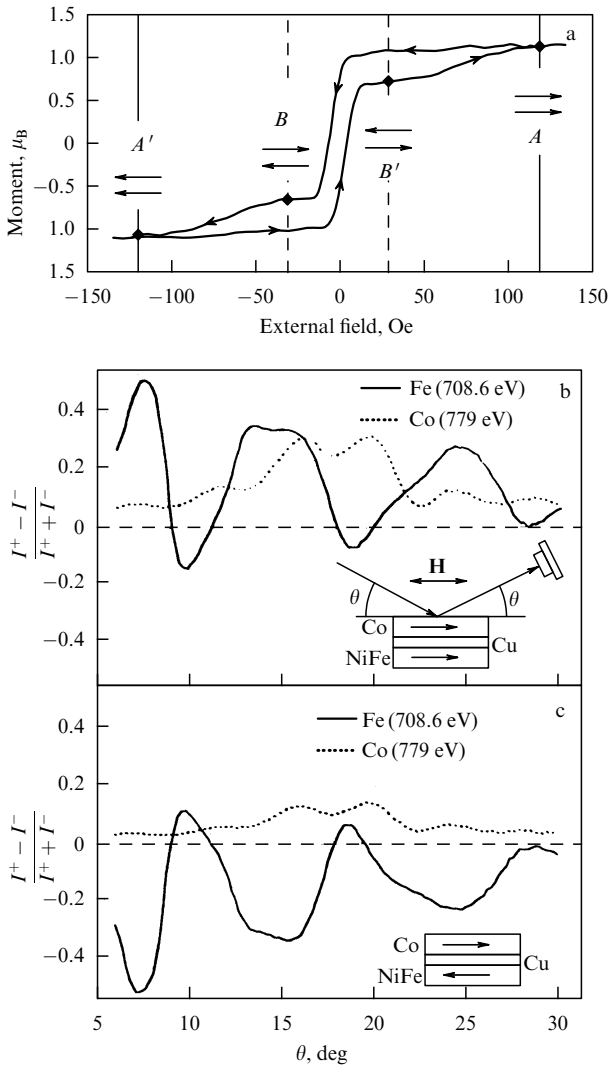

Figure 11. Two-step magnetization reversal of a NiFe/Cu/Co sandwich structure. The hysteresis loop is obtained with the use of a vibration magnetometer (a), the XRMS signal is measured in the vicinity of the L_3 edges of Co and Fe for the parallel (b) and antiparallel (c) orientations of layers individually [71].

presented in Fig. 11. The characteristic points A (A') in the static hysteresis loop correspond to a saturated state, when all layers are aligned with the magnetic field. In a magnetization-reversal process, when starting, for example, from the point A and directing the magnetic field oppositely to the magnetization, first the magnetization of the NiFe layer with its lower anisotropy reverses (point B') and only then the magnetic moments in the Co layer align along the field. XRMS spectra were acquired for the L_3 edge of Fe (708.6 eV) and the L_3 edge of Co (779 eV) in the cases when the magnetization vectors of the permalloy and cobalt layers were parallel and antiparallel to each other. It is seen that reversing the magnetization of the NiFe layer is accompanied by a change in the sign of the XRMS signal. Note that although the signal from the cobalt layer holds its sign, it decreases in magnitude, suggesting that these layers are not strictly antiparallel.

A combination of MCD and angular resolution in photoemission spectra allows one to study the dispersion of the peaks of dichroism and obtain information on the electronic band structure. For thin Ni films 15 monolayers (ML) thick on a Cu(100) substrate, such measurements not only showed good agreement with the calculated band structure, but also provided information on the interband hybridization [72]. For an ultrathin (3 ML) Co film on a

Cu(111) substrate, the band structure was found to be close to the bulk one [73]: the positive peak of the MCD signal corresponds to the spin-up subband, whereas the negative peak corresponds to the spin-down subband with an interband splitting of about 50 meV. An investigation of the fine structure of MCD spectra with angular resolution allowed the authors of Ref. [74] to reveal the effects of electron correlations in Ni and Co, but not in Fe. In ultrathin films and multilayer structures with thin layers, a growing role of strong correlations should be expected as compared to bulk crystals because of a decrease in the number of neighbors of a given layer and, as a consequence, of a decrease in the kinetic energy of electrons.

Many investigations of 'ferromagnetic metal – nonmagnetic metal' multilayer structures, for which the effective interaction between magnetic layers and the magnetic polarization of a nonmagnetic layer is of interest, were performed by the MCD method. For the Co(2 ML)/Pt(13 ML) system, it was found that only the first Pt layer bordering a Co layer is polarized appreciably ($\mu = 0.2\mu_B$), and the polarization of the second layer is smaller by an order of magnitude [75]. When measuring MCD near the Co $L_{2,3}$ and Cu $L_{2,3}$ edges of the Co(5 ML)/Cu(4 ML) system, these authors found an average magnetic moment of Cu ($0.014\mu_B$), whose value is in good agreement with the theoretical value $\mu(\mathrm{Cu}) = 0.0137\mu_B$ [9]. The orbital contribution is near-zero, so that the magnetic moment induced at Cu is a purely spin in nature. Additional information on the Co/Cu system was obtained by the authors of Ref. [76] who investigated MCD near the Co $M_{2,3}$ and Cu $M_{2,3}$ edges ($3p_{1/2,3/2} - 3d$ transitions). For the magnetic field perpendicular to the plane of the layers, magnetic signals were found not only for Co, but also for Cu, suggesting the presence of induced spin polarization of Cu near the interface owing to the exchange interactions of the 3d orbitals of Co and the 4s orbitals of Cu. For the Pd/Fe system, the MCD spectra near the white line of the $L_{2,3}$ absorption show that the structure of the Pd layer bordering the Fe layer differs from the FCC structure. The layer at the boundary is polarized with a moment $\mu(\mathrm{Pd}) = 0.4\mu_B$, and the orbital moment is small ($< 0.04\mu_B$). The thickness dependence of the MCD spectra allowed the authors of Ref. [77] to conclude that four Pd layers are polarized, that is, the magnetic boundary is thicker than the crystallographic one.

Highly nontrivial results were obtained by the MCD method in studies of Ce/Fe structures [54]. The existence of magnetic moments at the 4f electrons of Ce, for which the effects of strong electron correlations and strong hybridization with the conduction band are both possible together, was long in doubt. Formerly it was obtained using the MCD method for the $M_{4,5}$ absorption edges of Ce that in $CeFe_2$ the magnetic moment of 4f electrons is small ($0.1\mu_B$). Figure 12 shows MCD spectra near the $M_{4,5}$ absorption edges of Ce for two multilayer structures: Ce/Fe and La/Ce/La/Fe [54]. In these structures, Ce holds the structure of the α phase — a high pressure phase of bulk materials which is characterized by the strong hybridization of the 4f electrons with the conduction band. As is seen from Fig. 12, magnetic moments are associated with the 4f levels of Ce in the Ce/Fe structure. At the same time, the separation of Ce and Fe layers by an 0.5-nm La layer results in the vanishing of the 4f moments in Ce. Similar spectra for the $L_{2,3}$ absorption edges show that the magnetic moments of the 5d electrons of Ce hold when the Ce layers are separated by 0.5-nm La layers. This demonstrates the different depths of the 4f and 5d polarization in Ce

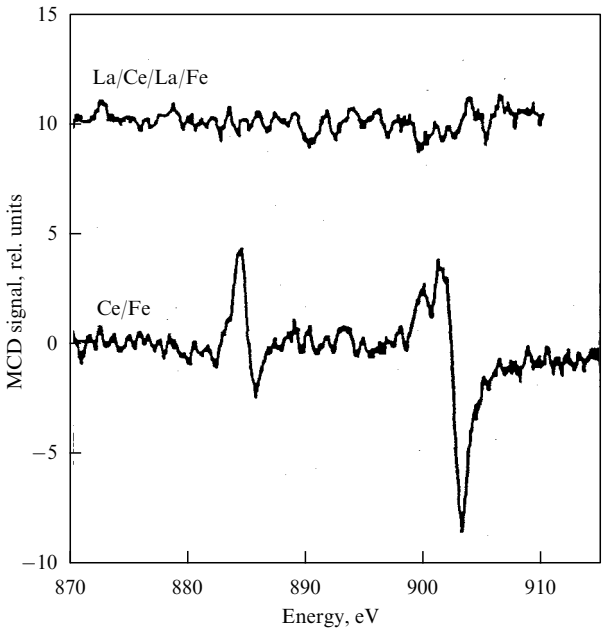

Figure 12. MCD spectra for the $M_{4,5}$ absorption edges of Ce in the Ce(1 nm)/Fe(3 nm) and La(0.5 nm)/Ce(1 nm)/La(0.5 nm)/Fe(3 nm) multilayer structures [54].

induced by the hybridization with the 3d electrons of Fe: the 4f polarization is localized at the Fe/Ce interface, whereas the 5d polarization propagates down to a depth of 2 nm from the interface.

For multilayer structures with sharply distinctive magnetic moments of layers, the magnetic moments at the interface are strongly dependent on the interface structure. For the Co/Cu system, for example, the ratio of the SPEXAFS amplitudes of Co and Cu arising from exchange scattering by the atoms of the first coordination shell must be equal to 7.3 for a sharp boundary and 1.9 for fully mixed Co and Cu layers. The results of measurements for a Co(5 ML)/Cu(4 ML) structure give a ratio which is close to 2.0, which indicates the strong mixing of layers at the interface [9].

Using the MCD method, two-dimensional Mn/Ni and Mn/Cu alloys were also investigated [78]. These alloys are formed by the evaporation of ultrathin (1/2 monolayer) Mn films on Cu(001) and Ni(001) surfaces. According to room-temperature low-energy electron diffraction data [79], these alloys are characterized by a (2×2) superstructure (Fig. 13). The ferromagnetic ordering of Mn atoms with a high

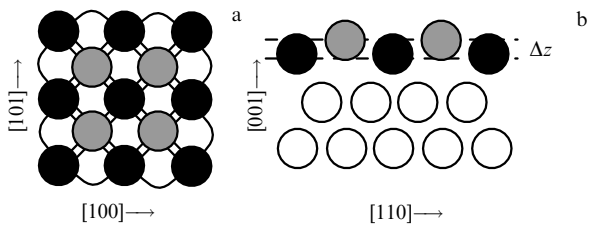

Figure 13. (2×2) superstructure of a surface alloy MnCu (MnNi): top view (a), side view (b). Dashed circles, Mn atoms; solid circles, Cu (Ni), layer 1; open circles, Cu (Ni), layers 2, 3. The displacement of the Mn atoms from the surface layer: $\Delta z = 0.03$ for MnCu, $\Delta z = 0.025$ for MnNi [78].

magnetic moment $\mu(\mathrm{Mn}) = 0.4\mu_B$ was predicted in paper [79]. Samples were prepared in a vacuum of $\sim 10^{-10}$ Torr, magnetized *in situ* by a field $H = 0.2$ T, and then MCD spectra were measured at room temperature. A comparison of the $L_{2,3}$ absorption spectra of Mn with the results of atomic calculations [80] has shown that the Mn^{2+} ion is in a high-spin state $S = 5/2$. The good agreement with atomic rather than band calculations is explained by the high degree of localization of the d electrons of Mn. First, for surface atoms, as is usually the case, the number of neighbors is less than for the volume ones; second, for these alloys the displacement of the Mn atoms located above the Cu(Ni) layer provides additional localization of the d electrons. For MnNi alloys, two types of samples were fabricated: on the Ni(001) substrate of an FCC crystal and on a thin Ni(2 ML) film grown on a Cu(001) single crystal. In the first case, the magnetic moment of the substrate is directed along the surface; in the second case, across the surface. In both cases, the MCD spectra of Mn and Ni near the $L_{2,3}$ absorption edges exhibit ferromagnetic ordering of Mn and Ni spins, which contrasts with the properties of a bulk MnNi crystal, which is antiferromagnetic at $T = 300$ K [81].

The high surface sensitivity of MCD in photoemission spectra was used for the study of the interface in multilayer structures with REM layers [82]. A two-layer structure Eu/Gd was prepared in a vacuum of $\sim 10^{-11}$ Torr through the deposition of high-purity REM from a vapor phase onto the surface of a W(110) single crystal. First a 10-nm Gd(0001) film and then (on the top of the Gd film) Eu films of different thicknesses were evaporated. For thin Eu films (less than 2 monolayers), the low-energy electron diffraction revealed a 6×6 hexagonal superstructure, which is destroyed at large thickness. MCD photoemission spectra were measured at $T = 25$ K and analyzed by resolving into the basis spectra (this method was suggested in Ref. [83]). The Gd 4f spectrum for the Eu/Gd structure coincided with the spectrum of the uncoated Gd(0001) film [82]; in other words, the magnetic properties of the interface on the Gd side was unaffected by the adsorption of Eu. Using the considerable chemical shift of the Gd and Eu spectra (about 6 eV), one can separate the 4f spectrum of Eu. For both orientations of the magnetization relative to the photon spin, the MCD spectrum for the Eu(2 ML)/Gd structure can be divided into two peaks, relating to the interface and the top layer of Eu, with a splitting of 0.7 eV between the peaks. The change in the spectra with changing the orientation of an external magnetic field points to the presence of a ferromagnetic structure in the Eu film in contrast to be bulk Eu, which is antiferromagnetic below 90 K.

4.5 Domain structure and magnetization-reversal dynamics

As is known, the X-ray scattering method used in studies of inhomogeneous systems is small-angle scattering, which allows one to determine the typical sizes of particles and the correlation lengths. The magnetic amplitude of small-angle scattering provides analogous information on the magnetic component of a material. An amorphous alloy $Gd_{25}Fe_{75}$ was investigated by this method in Ref. [75]. A clearly pronounced peak of the scattering intensity near the L_3 absorption edge of Gd for $q \sim 0.6$ nm^{-1} gives the value of the correlation length for Gd particles, $l_c \sim 10$ nm. According to the authors of the paper [75], the difference between the magnetic and non-magnetic scattering amplitudes in the small-q region is attributable to the existence of magnetic domains with characteristic dimensions of about 100 nm, which were directly observed with the help of a magnetic X-ray microscope. Magnetic X-ray microscopy is a combination of transmission microscopy and MCD [84]. For photon energies below the absorption edge of Fe, the space distribution of the MCD intensity is homogeneous, but at $\hbar\omega = 706$ eV, a structure shown in Fig. 14 arises. The domain wall width reaches the limiting value of spatial resolution (40 nm). The theoretical value of the width is $\delta = \pi(A/K)^{1/2} \sim 30$ nm, where A and K are the exchange interaction parameter and the anisotropy parameter, respectively. This result shows that the spatial-resolved MCD method, along with magnetic force microscopy, scanning electron microscopy with polarization analysis, and Lorentz transmission electron microscopy, allows one to study inhomogeneous structures, having at the same time the advantage of elemental sensitivity.

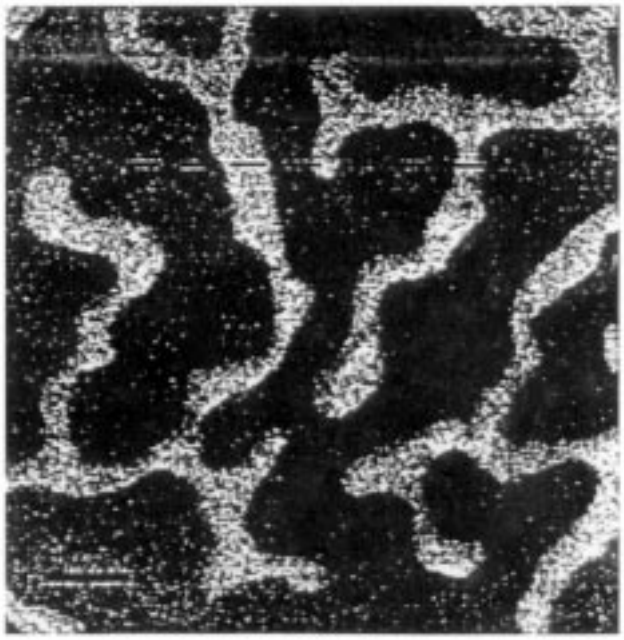

Figure 14. Magnetic domains in an amorphous alloy $Gd_{25}Fe_{75}$ observed near the L_3 absorption edge [75].

Another method of visualizing spatial magnetic structures with a resolution on the order of 50 nm uses a photoelectron emission microscope in which the MCD method is also used to obtain magnetic contrast [85]. For metal systems, the photoelectron escape depth in the process of inelastic photon scattering is about 2–3 nm. For permalloy $Fe_{19}Ni_{81}$ films 30 nm in thickness, the magnetic structures obtained for the Fe $L_{2,3}$ edge and the Ni $L_{2,3}$ edge are the same, and the regular form of domains is mainly formed under the influence of the shape and size of a sample, since the intrinsic anisotropy of permalloy is low. A different domain structure is observed for a polycrystalline multilayer Co/Pt structure grown on a Si substrate. The film was broken up into 20 μm × 20 μm squares by etching; the thickness of the film was 50 nm (Fig. 15). Owing to the strong magnetocrystalline anisotropy of Co and its random orientation in a polycrystalline sample, a complex irregular domain structure arises which is revealed from the MCD spectra near the L_3 absorption edge of Co.

Using the MCD method, it is possible to observe not only domains, but also domain walls. Since the MCD signal is proportional to $\boldsymbol{\varepsilon} \cdot \mathbf{M}$, where $\boldsymbol{\varepsilon}$ is the direction of the photon

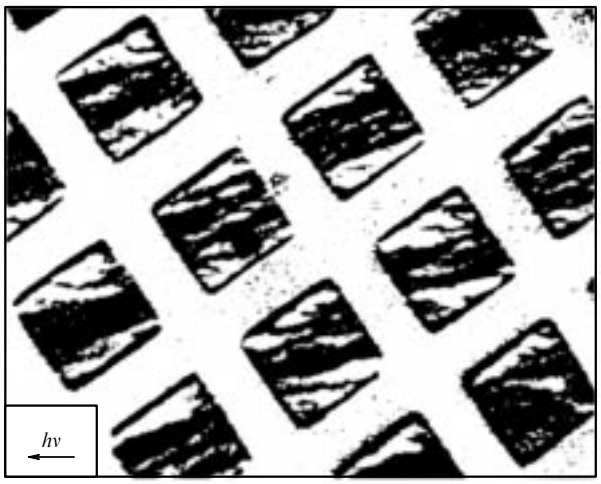

Figure 15. Domain structure of a Co/Pt multilayer system grown in 20×20 μm cells on the surface of a Si substrate [85].

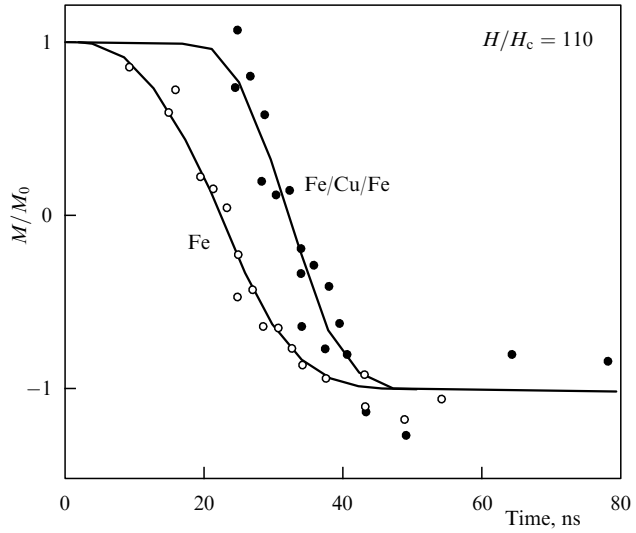

Figure 16. Magnetization-reversal dynamics for a Fe film and a Fe/Cu/Fe structure.

polarization and **M** is the magnetization, a domain whose magnetization is perpendicular to **ε** has no magnetic contrast. On the contrary, in a domain wall, where magnetic moments are rotated, the segments with **M** being parallel or antiparallel to **ε** will be shown up as light or dark lines. The magnetizations of adjacent domains are directed oppositely, and the vector **M** is rotated through 180° in the domain wall. In a bulk crystal such rotation would result in the appearance of a Bloch domain wall in which the rotation axis of the vector **M** is perpendicular to the plane of the wall. At a surface, such rotation is not advantageous from the energy standpoint, since at the center of the wall the vector **M** is perpendicular to the surface of the film. The rotation of **M** such that the vector **M** is invariably directed along the surface (Néel wall) is more advantageous. Thus, in the near-surface region, a change in the mode of rotation of the vector **M** occurs, which results in the appearance of magnetic singularities observed with the help of a photoemission MCD microscope [86].

In Ref. [54], an SR source with a pulse duration of 500 ps was used for the study of the time-resolved magnetization-reversal dynamics. Such investigations are of much interest for magnetic recording technology, since such an important parameter as the coercive force depends on the magnetization-reversal time. The typical values of the magnetization-reversal time are on the order of 10^{-8} s. Figure 16 illustrates the magnetization-reversal dynamics for two systems: a Fe film (1.5 nm) and a three-layer Fe (1.5 nm)/Cu (1.5 nm)/Fe (1.5 nm) structure. Magnetization reversal was performed in an external field being two orders of magnitude higher than the coercive field of the substrate H_c. As is seen from Fig. 15, the magnetization-reversal time for the three-layer structure is about 10 ns greater than that for the one-layer film. A difference in the steepness of curves in Fig. 16 indicates that the magnetization-reversal rate for the three-layer structure is higher than that for the one-layer film.

4.6 Orbital moments and their ordering in 3d-metal oxides

For partially occupied d shells, the main contribution to μ, as a rule, comes from spin moments, although an orbital contribution is also possible. Moreover, orbital moments can order with the formation of an orbital polarization, which essentially enriches the phase diagrams and physical properties. In this section, we will consider such effects for 3d-metal oxides.

A polarization analysis of the data on nonresonance magnetic X-ray scattering gives the ratio of the Fourier transforms of orbital and spin moments $L(Q)/S(Q)$. In the limit $Q \to 0$, this ratio enables one to determine the contribution of orbital moments in the total magnetization. For NiO, such an analysis revealed that in the antiferromagnetic phase the contribution of orbital moments to the total moment of a sublattice was equal to $17 \pm 3\%$ [87]; this markedly exceeds the value obtained in neutron experiments.

Orbital ordering in oxides is closely connected with charge and magnetic ordering. The latter is determined by the dependence of the effective exchange integral of super-exchange interaction on the mutual orientation of the occupied orbitals of adjacent ions (Goodenough – Kanamori rules). Consider the possibility of orbital ordering in $LaMnO_3$, a crystal with a perovskite structure, which has attracted considerable attention in connection with the discovery of the effect of giant magnetoresistance in solid solutions $La_{1-x}Sr_xMnO_3$ [88]. Here, the Mn^{3+} ion in the $3d^4$ configuration is located at the center of an oxygen octahedron whose crystal field splits the atomic d level into a t_{2g} triplet and a e_g doublet. According to Hund's rule, the ground state has the configuration $t_{2g}^3 e_g^1$, that is, one of the two e_g states, $d_{x^2-y^2}$ or $d_{3z^2-r^2}$, is occupied, so that the ground state is orbitally degenerate. One can introduce the concept of isospin, $I = 1/2$ in this case, and consider the orbital ordering as an isospin one. Lifting the degeneracy and ordering may be caused by the local deformations of the lattice (the Jahn – Teller effect), the quadrupole interaction of adjacent ions, or the dependence of the exchange integral on the orbital population.

The order parameter for orbital ordering is proportional to $\langle I^z \rangle \sim \langle d_\alpha^+ d_\alpha \rangle - \langle d_\beta^+ d_\beta \rangle$, where $d_{\alpha(\beta)}^+$ is the creation operator of a d electron on the orbital α (or β). In the case of more complex space structures (analogous to spiral spin structures), the quantity

$$\langle \hat{O}(q) \rangle = \sum_{\mathbf{R}} \exp(-i\mathbf{qR}) \sum_{\alpha\beta} c_{\alpha\beta} \langle d_\alpha^+ d_\beta \rangle_{\mathbf{R}}$$

can be selected as the order parameter. In the case of $LaMnO_3$, orbital ordering has to be accompanied by structural distortions, and it would appear reasonable that they may be found by standard crystallographic methods. However, in the related compound $La_{0,5}Sr_{1,5}MnO_4$, where the same distortions are expected, neutron scattering experiments have not revealed these distortions [89]. At the same time, resonance X-ray scattering allowed one to find orbital ordering in this compound [90], namely, the resonance enhancement of intensity for the wave vector $\mathbf{Q}_0$ near the K absorption edge of Mn, associated with $1s-4p$ transitions in Mn, was observed. The vector $\mathbf{Q}_0$ corresponds to charge ordering such that the lattice of the equivalent Mn ions is subdivided into sublattices of Mn^{3+} and Mn^{4+} ions. The charge-ordering temperature coincides with the orbital-ordering one, and both of these are about 100 K greater than the spin-ordering temperature. According to the interpretation of these results in paper [91], the orbital-ordering dependence of the scattering amplitude arises because of the splitting of unoccupied 4p levels by the crystal field, whose value is different for different occupations of the e_g levels. As a result, the denominator in formula (12) is different for ions with different occupation numbers of the $d_{x^2-y^2}$ and $d_{3z^2-r^2}$ levels, which leads to the modulation of the scattering vector $\mathbf{Q}_0$. Quantitative estimates of the effect were performed in the paper [91] on the basis of the atomistic approach to the description of 3d and 4p levels, but it is doubtful for 4p states because of their considerable delocalization.

5. Conclusion

In the last decade, X-ray magnetooptics has evolved into a powerful line of investigation which provides a large variety of methods based on the use of X-ray scattering and X-ray absorption for the determination of fine details of magnetic structures of bulk crystals, thin films, and surface layers. Being in a number of cases in competition with magnetic-neutronography methods, X-ray magnetooptics offers several undeniable advantages associated with the possibility of separating orbital and spin moments, the elemental sensitivity of the method, and the high resolution in k space.

The present review, which summarizes the results of magnetooptical studies of some magnetic materials, does not pretend to a complete description of the properties of concrete magnets. It merely provides some examples of using X-ray magnetooptics. Very recently, works have appeared on the application of infrared SR in the energy range of 0.01–1.5 eV and the first experiments on the investigation of 4f-electron systems by the MCD method have been performed [92]. The further progress of this method requires, along with experimental elaborations, a theoretical effort for describing the spectra observed, especially for spin-polarized EXAFS.

The study of domain structures and magnetization-reversal processes in domains is of vital technological importance. The process of controlled and reproducible creation of magnetic domains determines the properties of information recording and storage systems such as hard disks. At the present time the linear dimensions of the region containing 1 bit of information and the value of the magnetization-reversal time are on the order of 100 nm and $\sim 10^{-8}$ s, respectively. Therefore, a spatial resolution on the order of 10 nm and a time resolution of $\sim 10^{-9}$ s are required. As mentioned above, spatial resolution ~ 50 nm [84–86] and time resolution 0.5 ns [54] have been achieved. In the immediate future, one would expect further improvement in spatial resolution.

The materials considered in this review have been chosen not by accident. Magnetic multilayer systems are important elements of magnetic memory. The development of new memory devices with a large information recording density requires a knowledge of the fundamental magnetic parameters of materials. The Co/Pt and Co/Pd structures are being studied intensively along this line. Films with giant magnetoresistive effects, such as Co/Cu, Co/Cr or manganites on the basis of $LaMnO_3$, are of interest from the standpoint of their use in magnetoresistive recording heads. Therefore, there is no doubt that in the near future the above-discussed methods for the investigation of magnetic material with the use of synchrotron radiation will come out of research laboratories and find considerable industrial use.

The author is very grateful to G N Kulipanov for unceasing attention and assistance in the course of writing this review.

References

1. De Bergevin F, Brunel M *Phys. Lett. A* **39** 141 (1972)
2. Gibbs D et al. *Phys. Rev. Lett.* **61** 1241 (1988)
3. Hannon J P et al. *Phys. Rev. Lett.* **61** 1245 (1988)
4. Goedkoop J B et al. *J. Appl. Phys.* **64** 5595 (1988)
5. Schütz G et al. *Phys. Rev. Lett.* **58** 737 (1987)
6. Bohr J et al. *Physica B* **159** 93 (1989)
7. Brunel P M et al. *Acta Crystallogr. A* **39** 84 (1983)
8. Van der Laan G et al. *Phys. Rev. B* **34** 6529 (1986)
9. Schütz G et al. *J. Appl. Phys.* **76** 6453 (1994)
10. Gell-Mann M, Goldberger M L *Phys. Rev.* **96** 1433 (1954)
11. Platzman P M, Tzoar N *Phys. Rev. B* **2** 3556 (1970)
12. Babushkin F A *Dinamicheskaya Teoriya Magnitnogo Rasseyaniya Rentgenovskikh Lucheĭ v Antiferromagnetikakh* (Dynamical Theory of X-ray scattering in Antiferromagnets) (Leningrad: Izd. LGU, 1979)
13. Zhizhimov O L, Khriplovich I B *Zh. Eksp. Teor. Fiz.* **87** 547 (1984) [*Sov. Phys. JETP* **60** 313 (1984)]
14. Blume M *J. Appl. Phys.* **57** 3615 (1985)
15. Altarelli M *Elastic and Inelastic X-ray Scattering from Correlated Electrons: A Theoretical Perspective. Lecture at the 6th Summer School on Neutron Scattering* (Zuoz, Switzerland, 1998)
16. Hill J P et al. *Phys. Rev. Lett.* **66** 3281 (1991)
17. Schütz G et al. *Z. Phys. B* **73** 67 (1989)
18. Thole B T et al. *Phys. Rev. Lett.* **68** 1943 (1992); Carra P et al. *Phys. Rev. Lett.* **70** 694 (1993)
19. Schütz G et al. *Phys. Rev. Lett.* **62** 2620 (1989)
20. Avramov P V, Ovchinnikov S G *Zh. Eksp. Teor. Fiz.* **108** 1479 (1995) [*JETP* **81** 811 (1995)]
21. Avramov P V, Ovchinnikov S G *J. Phys. IV* (Paris) **7** 2 (1997)
22. Larson S *Chem. Phys. Lett.* **32** 401 (1974)
23. Larson S *Chem. Phys. Lett.* **40** 362 (1976)
24. Kosugi N et al. *Phys. Rev. B* **41** 131 (1990)
25. *Research Applications of Synchrotron Radiation* (BNL 50381) (Eds R Watson, M R Perlman) (1973)
26. *Vacuum Ultraviolet Radiation Physics* (Eds E Koch, R Haensel, C Kunz) Vol. 9 (New York: Pergamon, 1974)
27. Kulipanov G N, Skrinskiĭ A N *Usp. Fiz. Nauk* **122** 369 (1977) [*Sov. Phys. Usp.* **20** 559 (1977)]
28. Alferov D F, Bashmakov Yu A, Bessonov E G *Zh. Tekh. Fiz.* **46** 2392 (1976) [*Sov. Phys. Tech. Phys.* **21** 1408 (1976)]
29. Moiseev M V, Nikitin M M, Fedosov N I *Izv. Vyssh. Uchebn. Zaved. Fiz.* (3) 76 (1978)
30. Kulipanov G N, Mezentsev N A, Skrinsky A N *Rev. Sci. Instrum.* **63** 289 (1992)
31. Pengra D B et al. *J. Phys.: Condens. Matter* **6** 2409 (1994)
32. Stunault A et al. *J. Magn. Magn. Mater.* **140–144** 753 (1995)
33. McMorrow D F et al. *J. Magn. Magn. Mater.* **140–144** 779 (1995)
34. Ferrer S et al. *Phys. Rev. Lett.* **77** 747 (1996)

35. Watson B, Naushad A *J. Phys.: Condens. Matter*. **8** 361 (1996)
36. Chen C T et al. *Phys. Rev. B* **42** 7262 (1990)
37. Kulipanov G N, Skrinsky A N, Vinokurov N A *J. Synchrotron Rad.* **5** 176 (1998)
38. Kulipanov G N *Nucl. Instrum. Methods A* **303** 435 (1995)
39. Chernov V A et al. *Nucl. Instrum. Methods A* **405** 179 (1998)
40. Gerasimov R B et al. *J. Alloys Compd.* **252** 179 (1997)
41. Kim S K et al. *Appl. Phys. Lett.* **71** 66 (1997)
42. Kim S K, Koo Y M, Chernov V A *J. Phys. IV Colloq.* (Paris) **7** C2 1097 (1997)
43. Kim S K, Koo Y M, Chernov V A *J. Magn. Magn. Mater.* **170** L7 (1997)
44. Erskine J L, Stern E A *Phys. Rev. B* **12** 5016 (1975)
45. Chen C T, Smith N V, Sette F *Phys. Rev. B* **43** 6785 (1991)
46. Smith N V et al. *Phys. Rev. B* **46** 1023 (1992)
47. O'Brien W L et al. *J. Appl. Phys.* **76** 6462 (1994)
48. Tjeng L H et al. *Phys. Rev. B* **48** 13378 (1993)
49. Stearns M B, in *Numerical Data and Functional Relationships in Science and Technology* (Landolt – Börnstein Group 3, Vol. 19, Part A, Ed. H P J Wijn) (Berlin: Springer, 1986)
50. Eriksson O et al. *Phys. Rev. B* **45** 2868 (1992)
51. Söderlin P et al. *Phys. Rev. B* **45** 12911 (1992)
52. Schütz G et al., in *Proc. 2nd Europ. Conf. Progress in X-ray Synchrotron Radiation Research* Vol. 25 (Eds A Balerna, E Berrieri, S Mobilio) (Bologna: SIF, 1990) p. 229
53. Campbell I A *Proc. Phys. Soc. London* **89** 71 (1966)
54. Krill G *Synchr. Rad. News* **10** (3) 26 (1997)
55. Hill J P, Helgesen G, Gibbs D *Phys. Rev. B* **51** 10336 (1995)
56. Izyumov Yu A, Ozerov R P *Magnitnaya Neĭtronografiya* (Magnetic Neutron Diffraction) (Moscow: Nauka, 1966) [Translated into English (New York: Plenum Press, 1970)]
57. Vonsovskiĭ S V *Magnetizm* (Magnetism) (Moscow: Nauka, 1971) [Translated into English (New York: Wiley, 1974)]
58. Koehler W C et al. *Phys. Rev.* **151** 414 (1966)
59. Gibbs D et al. *Phys. Rev. B* **43** 5663 (1991)
60. Tang C C et al. *J. Magn. Magn. Mater.* **103** 86 (1992)
61. Helgesen G et al. *Phys. Rev. B* **52** 9446 (1995)
62. Bak P, Mukamel D *Phys. Rev. B* **13** 5086 (1976)
63. Krisch M N et al. *Phys. Rev. Lett.* **74** 4931 (1995)
64. Schütz G et al. *Rev. Sci. Instrum.* **60** 1661 (1989)
65. Garsia L M et al. *J. Appl. Phys.* **79** 6497 (1996)
66. Isaacs E D et al. *Phys. Rev. Lett.* **62** 1671 (1989)
67. Vettier C, in *Proc. 2nd Europ. Conf. Progress in X-ray Synchrotron Radiation Research* Vol. 25 (Eds A Balerna, E Berrieri, S Mobilio) (Bologna: SIF, 1990) p. 217
68. Rossat-Magnod J et al., in *Handbook on the Physics and Chemistry of the Actinides* Vol. 1 (Eds A J Freeman, G H Lander) (Amsterdam: North-Holland, 1984) Ch. 6
69. Nutall W J et al. *Phys. Rev. B* **52** 4409 (1995)
70. Perry S C et al. *Phys. Rev. B* **54** 15234 (1996)
71. Idzerda Y U, Chakarian V, Freeland J W *Synchr. Rad. News* **10** (3) 6 (1997); Langride S et al. *Phys. Rev. B* **55** 6392 (1997)
72. Kuch W et al. *Phys. Rev. B* **53** 11621 (1996)
73. Kuch W, Kirschner J *Synchr. Rad. News* **10** (3) 18 (1997)
74. Schneider C M et al. *Phys. Rev. B* **54** 15612 (1996)
75. Schutz G et al. *Synchr. Rad. News* **10** (4) 13 (1997)
76. Kawaguchi S et al., in *Abstr. 2nd Intern. Conf. Synchrotron Radiation in Material Science, Kobe, Japan* (1998) p. 56
77. Vogel J et al. *Phys. Rev. B* **55** 3663 (1997)
78. O'Brein W L, Tonner B P *J. Appl. Phys.* **76** 6468 (1994)
79. Wuttig M, Gauthier Y, Blügel S *Phys. Rev. Lett.* **70** 3619 (1993)
80. Van der Laan G, Thole B T *Phys. Rev. B* **43** 13401 (1991)
81. Pál L et al. *J. Appl. Phys.* **39** 538 (1968)
82. Starke K, Arenholz E, Kaindl G *Synchr. Rad. News* **10** (3) 16 (1997)
83. Thole B T, Van der Laan G *Phys. Rev. B* **44** 12424 (1991); **49** 9613 (1994)
84. Fischer P et al. *Z. Phys.* **101** 313 (1996)
85. Schneider C M et al. *Synchr. Rad. News* **10** (3) 22 (1997)
86. Schneider C M *J. Magn. Magn. Mater.* **175** 160 (1997)
87. Fernandez V et al. *Phys. Rev. B* **57** 7870 (1998)
88. Von Helmolt R et al. *Phys. Rev. Lett.* **71** 2331 (1993)
89. Steinlieb B J et al. *Phys. Rev. Lett.* **76** 2169 (1996)
90. Murakami Y et al. *Phys. Rev. Lett.* **80** 1932 (1998)
91. Ishihara S, Maekawa S *Phys. Rev. Lett.* **80** 3799 (1998)
92. Kimura S *Abstr. 2nd Intern. Conf. Synchrotron Radiation in Material Science, Kobe, Japan* (1998)